https://doi.org/10.5194/egusphere-2026-931
Preprint. Discussion started: 9 March 2026

Calibration of a coupled ice sheet-ocean model using observations of ice dynamics and basal melt in West Antarctica

Brad Reed[1], Jan De Rydt[1], Kaitlin A. Naughten[2], and Daniel N. Goldberg[3]

[1]School of Geography and Natural Sciences, Northumbria University, Newcastle upon Tyne, UK
[2]British Antarctic Survey, Cambridge, UK
[3]School of Geosciences, University of Edinburgh, Edinburgh, UK

Correspondence: Brad Reed (brad.reed@northumbria.ac.uk)

Abstract.

Coupled ice sheet-ocean models are increasingly used to investigate the complex interactions between ice dynamics and ocean forcing in West Antarctica, yet uncertainties in model parameters limit confidence in long-term sea-level projections. Among these parameters, ocean-model melt rates are typically calibrated using only basal melt observations for static ice-shelf geometries, neglecting feedbacks associated with evolving ice geometry, particularly in the Amundsen Sea sector.

Here, we calibrate a fully coupled ice sheet-ocean model using an ensemble of simulations constrained by spatial observations of basal melt rates and changes in ice speed and thickness over a historical period. This represents the first calibration to jointly incorporate oceanic and glaciological observations for optimizing melt-rate parameters. To match the historical observations of ice dynamical changes, the transient-coupled calibration favours parameter values that enhance basal melt near deep grounding lines, highlighting the sensitivity of ice dynamics to localized ocean forcing.

Using the historically-calibrated model, we provide century-scale projections of sea-level contribution under two scenarios: present-day control and warm RCP8.5 forcing. In the warm case, the transient-coupled calibration increases projected 2100 sea-level rise by 14 mm relative to a melt-only calibration. This exceeds the 7 mm difference simulated between the two climate scenarios. These findings underscore the critical importance of jointly validating against oceanic and glaciological observations in model calibration.

1 Introduction

Since 1992 the Antarctic Ice Sheet has lost more than 2,600 gigatonnes of ice, equivalent to 7.4 mm of global sea-level rise, with over 89 % of this loss originating from West Antarctica (Otosaka et al., 2023). The largest imbalance occurs in the Amundsen Sea sector (Rignot et al., 2019; Smith et al., 2020), where glaciers have sped up (Davison et al., 2023b) in response to ocean-driven melting and calving of their floating ice shelves (Greene et al., 2022; Davison et al., 2023a). This has driven widespread retreat (Rignot et al., 2014; Konrad et al., 2018; Milillo et al., 2022) and thinning (Shepherd et al., 2019; Nilsson et al., 2022) of grounded ice in a region with the potential to raise global sea level by up to 126 cm (Rignot et al., 2019). Ice-shelf melting is projected to increase under all greenhouse gas emissions scenarios (Naughten et al., 2023; Coulon et al., 2024), making it essential to understand how ice-ocean interactions are represented in sea-level projections (Edwards et al.,

https://doi.org/10.5194/egusphere-2026-931
Preprint. Discussion started: 9 March 2026

2021; Lowry et al., 2021; Coulon et al., 2024). Here, we use a fully coupled ice sheet-ocean model to examine how calibrating basal melt rates using both oceanic and ice-dynamical observations influences simulated ice evolution and sea-level projections in the Amundsen Sea sector.

Accurately representing these ice-ocean interactions requires understanding the oceanographic processes that drive ice-shelf basal melt. Along the Amundsen Sea coastline, floating ice shelves are exposed to modified Circumpolar Deep Water (mCDW), which drives intense basal melting within their cavities (Jacobs et al., 1996). This warm, saline water is transported onto the continental shelf via a shelf-break undercurrent (Walker et al., 2013; Jenkins et al., 2016) and funnelled through deep bathymetric troughs (Nakayama et al., 2018; Dinh et al., 2024), producing melt rates up to 100–200 m yr^{-1} at deep grounding lines (Dutrieux et al., 2013; Milillo et al., 2019; Shean et al., 2019). The heat available for melting is thus influenced by the strength of the undercurrent (Jenkins et al., 2016; Kimura et al., 2017; Dotto et al., 2019), which varies on monthly timescales with shelf-break winds (Dotto et al., 2020) and on decadal timescales with cross-shelf density gradients driven by sea-ice freshwater fluxes (Silvano et al., 2022; Haigh et al., 2026). Positive feedbacks amplify these processes: increased melt strengthens density gradients and intensifies cavity circulation (Jourdain et al., 2017; Haigh and Holland, 2024), enhancing heat transport beneath ice shelves and leading to higher melt rates (Donat-Magnin et al., 2017; Holland et al., 2023). On longer centennial timescales, atmospheric warming and precipitation are predicted to be the primary driver of undercurrent acceleration, via decreased sea-ice formation and transport, leading to further oceanic warming and melting (Turner et al., 2025).

Basal melting, calving, and fracturing weaken ice shelves and reduce their ability to buttress upstream grounded ice, promoting flow acceleration and grounding-line retreat (Dupont and Alley, 2005; Gagliardini et al., 2010; Gudmundsson et al., 2019; Sun and Gudmundsson, 2023). This effect is strongest for laterally confined shelves or those pinned at bathymetric highs. As a result, future ice loss is likely to be particularly sensitive to melting near grounding lines, shear margins, and pinning points (Favier et al., 2016; Reese et al., 2018; Goldberg et al., 2019; Morlighem et al., 2021). Accurately modelling this sensitivity requires realistic basal melt rates, yet ice-sheet models often rely on parametrized melt formulations. While computationally efficient, commonly used schemes underestimate melt rates near the grounding lines (Favier et al., 2019; Burgard et al., 2022) and cannot capture feedbacks between evolving ice-shelf geometry, ocean circulation, and bathymetry as ice retreats (De Rydt et al., 2014; Seroussi et al., 2017), potentially biasing projections of future ice loss.

Coupled ice sheet-ocean models are used to examine feedback processes in high-resolution regional domains, overcoming the limitations of ice-sheet melt parameterizations (e.g., Seroussi et al., 2017; Goldberg and Holland, 2022; Bett et al., 2024; De Rydt and Naughten, 2024). In these frameworks, basal melt rates are computed by the ocean model and passed to the ice sheet model to update ice-shelf geometry throughout the simulation. Although these models are coupled together to simulate dynamical ice-shelf feedbacks, they have, to date, been initialized and calibrated separately using a step-wise approach (e.g., Seroussi et al., 2017; Naughten et al., 2021; De Rydt and Naughten, 2024; Richter et al., 2025). This separation can introduce a transient adjustment, or 'shock', associated with mass imbalance when the models are first coupled. Contributing to this shock, ocean model melt-rate parameters are typically tuned against observations assuming a static ice-shelf geometry (Goldberg and Holland, 2022), thereby neglecting the evolving ice geometry that influences cavity circulation and melt patterns. This

https://doi.org/10.5194/egusphere-2026-931
Preprint. Discussion started: 9 March 2026

approach further assumes that 'observed' melt rates, commonly inferred from satellite-derived thinning, are reliable, despite large uncertainties in regions that exert strong control on ice-sheet stability, particularly near the grounding line (Fricker et al., 2009). The ice sheet component also contributes to the coupling shock, as the initial state is typically generated through data assimilation or spin-up methods, which can result in divergent long-term responses of grounded ice to changes in basal melting (Seroussi et al., 2019).

These limitations motivate the need for a more integrated calibration strategy. A more robust calibration of coupled ice sheet-ocean models therefore requires combining multiple observational constraints, including both melt rates and ice dynamics, over a transient period to better capture the evolving state of the system. It remains unclear, however, how such an approach influences long-term simulations and whether it can reduce the large uncertainties associated with basal melting in sea-level projections (Edwards et al., 2021).

In light of the above, this study had three objectives: (1) to deliver the first historically calibrated coupled ice sheet-ocean model using all available measurements of ice-shelf melt rates and changes in ice speed and thickness between 2013 and 2017; (2) to provide new data-driven evidence for the importance of accurately simulating basal melt near the grounding lines; and (3) to provide century-scale projections of mass loss under different climate scenarios using the calibrated model.

The paper is organised as follows. Section 2 describes the ice and ocean models and their coupling framework, along with the model initialization procedures. This section also outlines the experiment setup, which includes an ensemble of hindcast coupled simulations used for model calibration, and a subset of simulations extended to 2100 under two different climate scenarios: present-day control and warm RCP8.5. Section 3 presents results from the hindcast ensemble and calibration, while Sect. 4 gives the long-term response of the ice sheet. Section 5 discusses limitations and future outlook.

2 Methods

We used the coupled ice sheet-ocean model Úa-MITgcm (Naughten et al., 2021; De Rydt and Naughten, 2024) with a new calibration approach for ocean-model melt parameters constrained by multiple observations. The calibration integrated satellite observations of ice-sheet thinning, flow acceleration, and basal melt rates over an approximate hindcast period of 2013–2017 (see Sect. 2.4 and Table 2). While the various datasets used for model geometry, initialization, coupling, forcing, and calibration do not all cover identical time periods, they represent the best available and most widely used observations and products closest to this target hindcast window. This period is particularly suitable for calibration because velocity changes were not dominated by large calving events (e.g., Joughin et al., 2021; Sun and Gudmundsson, 2023), processes not included in our model, allowing us to isolate the dynamic response to basal melting. Using the calibrated model, we investigated the impact of this calibration on projected ice loss through 2100.

The ice-flow model Úa (Gudmundsson et al., 2012) was used to simulate the time-evolving ice dynamics and a description of its setup and initialization procedure is given in Sect. 2.1. The ocean circulation for the Amundsen Sea region was simulated with the Massachusetts Institute of Technology general circulation model (MITgcm) (Marshall et al., 1997), which included components for the sea ice and ice-shelf thermodynamics (Losch, 2008). A brief summary of the model setup is given in

https://doi.org/10.5194/egusphere-2026-931
Preprint. Discussion started: 9 March 2026

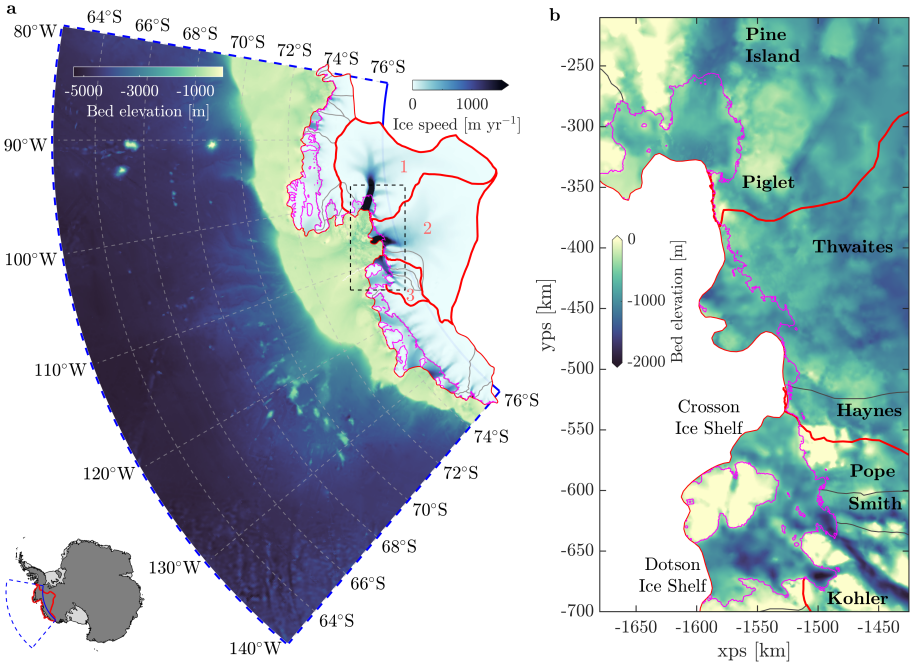

Figure 1. (**a**) Full model domains for MITgcm (ocean) and Úa (ice). Background colours indicate bathymetry and modelled ice speed, shown with separate colour maps. Dashed blue edges show MITgcm open boundaries at 80°W, 140°W, and 62°S, and the solid blue line shows the closed southern boundary at 76°S. Thin red lines show the outline of the full Úa domain, which is overlaid by thicker red lines to show the key basins that are analysed in this study: (1) Pine Island Glacier (PIG), (2) Thwaites Glacier (THG), and (3) Pope-Smith-Kohler Glaciers (PSK). Thin grey lines show individual glacier basins from Mouginot et al. (2017c) and pink lines indicate the modelled grounding-line position using BedMachine Antarctica v3 geometry data (Morlighem et al., 2020). Inset shows the location of the model domains within Antarctica. (**b**) Zoomed-in view of the sub-ice bed elevation for the three main basins in the dashed box shown in **a**.

Sect. 2.2, with a more detailed description provided by Naughten et al. (2022). The coupling framework between Úa and MITgcm is summarised in Sect. 2.3; further details can be found in Naughten et al. (2021) and De Rydt and Naughten (2024). The experimental setup is described in Sect. 2.4 with details about the model calibration procedure and forecast simulations.

2.1 Ice-flow model

2.1.1 Úa domain and numerical setup

Úa is a finite-element ice-flow model that solves the vertically-integrated shallow ice-stream approximation (SSTREAM or SSA; Macayeal, 1989) on an unstructured grid of linear triangles. The full model domain included both floating ice (92,000 km^2) and grounded ice (622,000 km^2) for all drainage basins in the Amundsen Sea Sector (Fig. 1a). However, the main analysis in the following sections focuses on the basins experiencing the highest rates of mass loss (Smith et al., 2020). To be consistent with previous studies, these have been grouped into the following regions: (1) Pine Island Glacier (PIG), (2)

https://doi.org/10.5194/egusphere-2026-931
Preprint. Discussion started: 9 March 2026

Thwaites Glacier (THG), and (3) Pope-Smith-Kohler (PSK) (Fig. 1). The inland boundary was defined by the outer ice divides of the drainage basins (Mouginot et al., 2017c), while the seaward boundary followed the coastline contour from the BedMachine Antarctica v3 ocean mask (Morlighem et al., 2020). Ice fronts were fixed for all simulations and there was an imposed Neumann boundary condition for ocean pressure. Along the grounded boundary, a zero velocity Dirichlet boundary condition was assumed.

The mesh grid used by Úa was generated in three stages to ensure finer resolution was located in regions of rapid deformation and near the grounding line. Strain rates indicate where ice deformation is strongest and finer resolution required, but direct estimates from velocity measurements are noisy. Therefore, we first used an initial coarse mesh (4–10 km node spacing) to model approximate ice velocities and derive smoother strain rates. Then, areas of strong strain-rate gradients were refined to 0.5–1 km, while coarser elements of 5–8 km were used for the slower-flowing inland regions. During forward simulations, the mesh was further refined to a resolution of 100 m within 1 km of the grounding line, and then coarsened again once the grounding line migrated away from those areas. This mesh adaptation around the grounding line was updated monthly in regions where ice velocities were greater than 500 m yr^{-1}. The mesh that was used in the forward simulations had approximately 464,000 elements and 234,000 nodes, with mean nodal spacing of 1.1 km and a minimum of 100 m. All meshes were generated with the *mesh2d* software (Engwirda, 2014).

The initial ice-sheet surface elevation, ice thickness and bed elevation were from BedMachine Antarctica v3, which incorporates data between 1970 and 2019 but has an effective timestamp of 2015 (Morlighem et al., 2020). However, sub-shelf bed topography remains highly uncertain in some regions, particularly beneath Pine Island Ice Shelf, where the BedMachine dataset produces a thin and relatively uniform water column downstream of the main grounding line. This makes the ice shelf susceptible to rapid, artificial re-grounding if melt rates are even slightly underestimated. To mitigate this, we modified the bathymetry beneath the ice shelf in areas where BedMachine relies on interpolation or hydrostatic assumptions. The modified region begins approximately 10 km downstream of the main grounding line, in an area that was previously a grounded ice plain. In this area, the BedMachine bathymetry was replaced with the bed topography from Dutrieux et al. (2014), resulting in a deepening of 200–300 m, which remains within estimated bed uncertainties. No changes were made to the grounding-line bed or to upstream regions.

Úa uses spatially varying, depth-averaged ice densities, calculated from the firn depth correction and ice thickness provided by BedMachine Antarctica v3 (Morlighem et al., 2020; Schelpe and Gudmundsson, 2023). A spatially varying snow-accumulation rate from the RACMO2.3 climatology for the period 1979–2013 was prescribed in all simulations (Melchior Van Wessem et al., 2018). Ice rheology was described by Glen's flow law with an exponent $n = 3$ and a spatially varying rate factor A which represents ice viscosity. Basal sliding is represented by a non-linear Weertman sliding law with exponent $m = 3$ and a spatially varying basal slipperiness parameter C. Both A and C were assumed to be time-independent, an approximation we consider reasonable over the relatively short calibration window. These parameters were inferred through an inversion procedure described in Sect. 2.1.2.

At each coupling timestep, updated basal melt rates were obtained from the ocean model (Sect. 2.2.2) and prescribed at all floating nodes in Úa. In the finite element framework, these nodal values are interpolated within elements and evaluated

https://doi.org/10.5194/egusphere-2026-931
Preprint. Discussion started: 9 March 2026

at integration points using the shape functions. As a result, for elements that contain the grounding line (the location where the height above floatation becomes zero), integration points upstream of the grounding line can receive non-zero melt rates. However, given the small nodal separation (100 m) near the grounding line, the area over which melt can leak across the grounding line is negligible.

2.1.2 Initialization of Úa

Initial modelled ice velocities were generated using an inverse method with data assimilation that estimates the unknown spatial fields for model parameters C and A in the basal sliding and flow laws. The initialization is a critical step in ice-flow modelling, as it can influence the simulated evolution of the ice sheet (Seroussi et al., 2019) and can account for over half of the uncertainty in sea-level projections (Rosier et al., 2025). A summary of the method that we used is provided here, with full details in Appendix A.

The initialization procedure comprised three stages. First, we performed an inversion using observed ice velocities and associated measurement errors from the MEaSUREs InSAR mosaic, which incorporates data mostly between 2006 and 2016 (Mouginot et al., 2017b; Rignot et al., 2017). This step minimized the misfit between modelled and observed velocities (Eq. A1) subject to a regularisation term (Eq. A2). Although this resulted in a good fit to present-day ice flow, it left the rate of thickness change unconstrained, which can lead to unrealistically large values of ice-thickness changes at the start of a transient simulation (Fig. A1b). To mitigate this, the second stage involved a short five-year transient relaxation period to dampen these artificial thickness changes arising from data inconsistencies. During this relaxation, we used the output from the initial inversion and kept the ice shelf thickness constant by applying a diagnostic basal melt rate (Eq. B1), which also ensured the grounding line remained unchanged. After this period, thickness changes in grounded ice remained within the uncertainties of the bed elevation dataset, with a median change of -1.8 m. Finally, a second inversion was carried out, incorporating an additional constraint of observed ice-thickness changes (Eq. A3) between 2013 and 2017 from Shepherd et al. (2019). This yielded an initial state that captured the approximate modern-day ice flow and pattern of thinning.

Several aspects of the model setup and initialization described above were implemented to prevent unrealistic grounding-line advance at the start of the subsequent hindcast and forward simulations: (1) using high mesh resolution around the grounding line in the fastest-flowing regions; (2) applying basal melt to all floating nodes; (3) including a short relaxation period and a thickness-change inversion; and (4) a small modification to the bed elevation downstream of the Pine Island grounding line.

2.2 Ocean model

2.2.1 MITgcm domain and numerical setup

MITgcm is a numerical geophysical model that solves the three-dimensional Navier-Stokes equations; in this study it was used with the hydrostatic and Boussinesq approximations, to simulate regional ocean circulation and thermohaline properties of the Amundsen Sea. The model is configured on an Arakawa C grid with polar stereographic coordinates. The model domain, adapted from Naughten et al. (2022), encompasses the deep ocean, continental shelf and ice-shelf cavities (Fig. 1a), with open

https://doi.org/10.5194/egusphere-2026-931
Preprint. Discussion started: 9 March 2026

boundaries at 80°W, 140°W, and 62°S. The closed southern boundary at 76°S included grounded ice to allow for retreat in the coupled simulations. The horizontal resolution is 0.1 degree (2–5 km) and there are 50 vertical z-layers with varying thickness from 10 m at the surface to 300 m at depth. A timestep of 300 s was used in all simulations.

The bathymetry was from BedMachine Antarctica v3 (Morlighem et al., 2020) with the aforementioned adjustment downstream of Pine Island Glacier grounding line (see Sect. 2.1). The model also assumes a line of grounded ice bergs along Bear Ridge (Fig. 1a), which blocks shallow coastal currents and alters sea-ice advection patterns, both of which have an important impact on the oceanography in the region (Bett et al., 2020).

Basal melt rates were calculated using a modified version of the default MITgcm implementation, enabling us to test the sensitivity to intensified melting in the deep cavities relative to the canonical melt rate formulation. Further details are provided in the next section (Sect. 2.2.2). Forcing at the surface and along the open ocean boundaries for all experiments is described in Sect. 2.4. The open boundary conditions were applied over a sponge layer of five grid points, with a relaxation time of 1 day at the outermost point and 5 days at the innermost point. In all MITgcm simulations, a monthly correction was applied to the velocity boundary conditions to prevent drift in ocean volume and sea surface height (Naughten et al., 2021). All other parameters and parameterizations, including for the sea ice module, follow Naughten et al. (2022).

2.2.2 Modified melt-rate parameterization

In MITgcm, melt rates beneath the ice shelf are commonly calculated using the 'three-equation model' (Holland and Jenkins, 1999; Losch, 2008), which evaluates turbulent fluxes of heat and salt across the ice-ocean boundary layer. In this parameterization, the turbulent exchange coefficients can be assumed to be constant (e.g., $\gamma_T = 1\times10^{-4}$ m s^{-1} and $\gamma_S = 5.05\times10^{-7}$ m s^{-1} in Losch (2008)), or, as discussed by Holland and Jenkins (1999) and Dansereau et al. (2014), a more physical-based approach is to approximate them with a function of the friction velocity u_* (McPhee et al., 1987)

$$\gamma_{T,S} = \frac{u_*}{\Gamma_{\text{Turb}} + \Gamma^{T,S}_{\text{Mole}}}, \tag{1}$$

where u_* at the ice-ocean interface is approximated by a linear function of the mixed-layer velocity U_M and a dimensionless drag coefficient C_d,

$$u_*^2 = C_d U_M^2. \tag{2}$$

However, in z-coordinate ocean models, such as MITgcm, the combination of coarse horizontal and vertical resolution can introduce multiple issues in simulating basal melt. First, the discretization can produce a step-like melt-rate pattern because the first open cells beneath the ice base are not necessarily horizontally connected, and thermohaline properties in those cells can become discontinuous. This issue occurs throughout the cavity. Second, coarse vertical resolution, particularly in regions of thin water column near the grounding line, can prevent overturning circulation from being adequately resolved, leading to uncertainties in local melt rates (Dansereau et al., 2014; Gwyther et al., 2020). These errors can propagate in coupled simulations, affecting ice-shelf geometry and grounded ice evolution (Seroussi et al., 2017; Goldberg et al., 2019).

https://doi.org/10.5194/egusphere-2026-931
Preprint. Discussion started: 9 March 2026

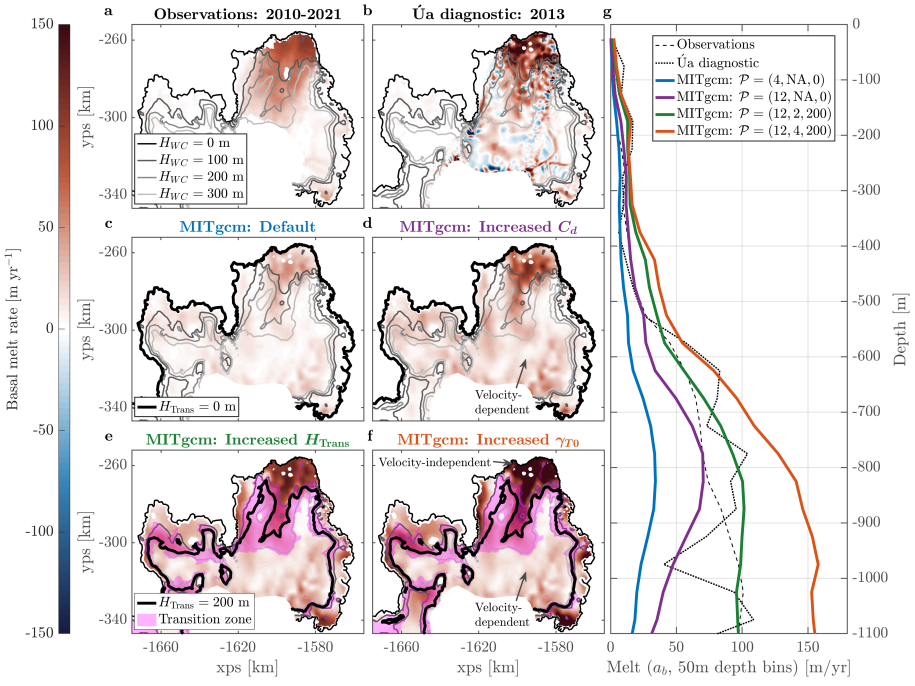

Figure 2. Pine Island Glacier basal melt rates shown as spatial fields (**a**-**f**) and depth curves (**g**) from: CryoSat surface elevation change between 2010 and 2021 (Gourmelen et al., 2025) (**a**, dashed black in **g**), Úa mass conservation (Eq. B1) for the initial ice geometry (**b**, dotted black in **g**), and four MITgcm model simulations (**c**-**f**, colours in **g**). The default MITgcm velocity-dependent melt-rate parameterization, where $H_{\mathrm{Trans}} = 0$ m in Eq. (4), is shown for two different drag coefficients: $C_d = 4 \times 10^{-3}$ (**c**, blue) and $C_d = 12 \times 10^{-3}$ (**d**, purple). The modified melt parameterization with $H_{\mathrm{Trans}} = 200$ m is shown for two different heat transfer coefficients: $\gamma_{T0} = 2 \times 10^{-4}$ m s^{-1} (**e**, green) and $\gamma_{T0} = 4 \times 10^{-4}$ m s^{-1} (**f**, orange). In panels **a**-**f**, water column thickness (H_{WC}) contours are shown as thin grey lines (0:100:300 m), while the transition zone and centre point between velocity-dependent and independent melt-rate parameterizations is shown in shaded pink and thick black, respectively. In the legend of panel **g**, a short-hand notation indicates which parameter values are used in the modified melt parameterization: $\mathcal{P} = (C_d, \gamma_{T0}, H_{\mathrm{Trans}})$.

Figure 2c shows the melt-rate distribution beneath Pine Island Ice Shelf simulated by MITgcm for present-day ocean conditions using melt parameters from Naughten et al. (2022). Compared with satellite-derived estimates (Fig. 2a) and melt rates computed from mass conservation in the ice-sheet model (Fig. 2b; Appendix B), the default MITgcm melt parameterization (blue line in Fig. 2g) underestimates melt in the deeper regions (below -400 m) near the main grounding line. One common approach to address this is increasing the drag coefficient C_d in Eq. (2) to elevate grounding-line melt rates (Jourdain et al., 2017; Goldberg et al., 2019; Bett et al., 2024). However, this scales up melt rates everywhere, which may produce unrealistically high melt in shallower regions while still underestimating deep melt (Fig. 2d).

To overcome the bias of low melt rates near the grounding line, we used an alternative approach by applying a modified form of the melt-rate parameterization. This alternative formulation uses constant exchange velocities (γ_{T0}, γ_{S0}) in regions of

https://doi.org/10.5194/egusphere-2026-931
Preprint. Discussion started: 9 March 2026

narrow water columns, i.e., close to the grounding line where circulation is poorly resolved, and velocity-dependent exchange (γ_T, γ_S) elsewhere:

$$\gamma_{T\mathrm{mod}} = \Lambda_{\mathrm{Trans}}\gamma_T + (1 - \Lambda_{\mathrm{Trans}})\gamma_{T0}, \tag{3}$$

with an analogous expression for $\gamma_{S\mathrm{mod}}$, but with $\gamma_{S0} = 5.05 \times 10^{-3}\gamma_{T0}$. Following Hellmer and Olbers (1989); Losch (2008); Jenkins et al. (2010), we prescribe this canonical ratio between γ_{S0} and γ_{T0} in regions where constant exchange velocities are applied. In the above expression, Λ_{Trans} is a dimensionless parameter between 0 and 1 that controls the transition between the two regimes. It depends on the local water column thickness (H_{WC}) and a prescribed transition thickness (H_{Trans})

$$\Lambda_{\mathrm{Trans}} = \frac{1}{2} + \frac{1}{2}\tanh\left(\frac{H_{\mathrm{WC}} - H_{\mathrm{Trans}}}{H_{\mathrm{Trans}}/4}\right). \tag{4}$$

In the limit $H_{\mathrm{Trans}} = 0$, Eq. (4) reduces to $\Lambda_{\mathrm{Trans}} = 1$ and we recover the default melt-rate parameterization with $\gamma_{T\mathrm{mod}} = \gamma_T$ (Fig. 2c,d). For $H_{\mathrm{Trans}} > 0$, Λ_{Trans} varies smoothly from 0 for $H_{\mathrm{WC}} < H_{\mathrm{Trans}}$ to 1 for $H_{\mathrm{WC}} > H_{\mathrm{Trans}}$. Figure 2e–f illustrates the modified parameterization for $H_{\mathrm{Trans}} = 200$ m. Melt rates transition from velocity-independent close to the grounding line, to velocity-dependent in regions with thicker water columns. Most of this transition (Λ_{Trans} varying between 0.002 and 0.99) occurs within the pink highlighted region in the figure, corresponding to H_{WC} between 50 m and 350 m and centred around $H_{\mathrm{WC}} = 200$ m.

As opposed to the default melt parameterization, with C_d as its only tunable parameter, the modified melt-rate formulation has three tunable parameters, $\mathcal{P} = (C_d, \gamma_{T0}, H_{\mathrm{Trans}})$. Each of these has a distinct impact on the spatial distribution of melt in the cavities, as shown in Fig. 2. As previously mentioned, a higher C_d value increases melt rates across the entire ice shelf (Fig. 2d), whilst a higher H_{Trans} value widens the region over which a velocity-independent melt rate is applied (Fig. 2e), and a higher γ_{T0} value increases the melt in the thin water column region (Fig. 2f). The latter two parameters alter the spatial pattern of melting, allowing for a concentration of higher melt near the grounding lines, as shown by the greater increases in deep melt rates below -400 m (Fig. 2g). These are the three parameters that we calibrate using joint observations of melt rates and ice dynamics, as described in Sect. 2.4.2.

2.3 Coupled system

At monthly time steps, the ocean and ice models were coupled offline and advanced simultaneously, exchanging basal melt rates and ice geometry with a one-month time lag. Over each monthly interval, MITgcm computed basal melt rates for ice shelves assuming a fixed geometry, while Úa evolved the ice geometry using the corresponding monthly integrated melt rates. Because the two models have different grids, exchanged fields were linearly-interpolated between them. Melt rates were held constant over the month and extrapolated by nearest neighbour into any newly floating areas, which were expected to be small on these timescales. At the end of each coupling interval, the updated ice-shelf draft from Úa was passed to MITgcm for the next interval, with temperature and salinity horizontally extrapolated into newly opened ocean cells and a velocity correction applied to preserve barotropic transport. At each coupling time step, both models were restarted from their previous thermodynamic states. As in previous studies (Naughten et al., 2021; De Rydt and Naughten, 2024), we applied a small, temporary correction

https://doi.org/10.5194/egusphere-2026-931
Preprint. Discussion started: 9 March 2026

to the MITgcm bathymetry at each coupling timestep to ensure that neighbouring water columns remain connected by at least two partial wet cells in the vertical. Two cells are required to ensure connectivity for all model quantities, due to MITgcm's Arakawa C-grid. The bathymetry was adjusted by the minimum amount to achieve this aim, making use of MITgcm's partial cell capability, and only a small number of grid cells near the grounding line required this correction. This modification is fully reversible in the sense that it does not affect Úa and is recalculated independently at every coupling timestep, so no permanent changes to the bathymetry accumulate over time.

The coupling framework which is written in Python, together with MITgcm and a compiled Úa MATLAB code were all run on the UK high performance computer ARCHER2.

2.4 Experiment setup

The first aim of our work was to calibrate the three melt-rate parameters $\mathcal{P} = (C_d, \gamma_{T0}, H_{\mathrm{Trans}})$, introduced in Sect. 2.2.2, using a comprehensive set of hindcast simulations and data sources (Table 1 and Fig. 3). We began this process with a two-stage ocean-only spin-up (SPIN_CTR and SPIN_VAR_CTR, Sect. 2.4.1), followed by an ensemble of coupled simulations over a hindcast period (HIND_CTR, Sect. 2.4.2) between 2013 and 2017 with different combinations of the melt-rate parameters. The ensemble simulations were then ranked according to their agreement with all available observations, and their associated uncertainties. These included ice-shelf melt rates as well as spatial patterns of ice speed and thickness changes over the same period. The optimal parameter values obtained through this transient-coupled calibration (TR) approach were compared with those derived from an ad-hoc tuning using a static ice-shelf geometry in which only melt-rate observations were used (ST), as is common practice in ice shelf-ocean and ice sheet-ocean simulations (Jenkins et al., 2010; Dansereau et al., 2014; Nakayama et al., 2017; Jourdain et al., 2017; Goldberg et al., 2019; Naughten et al., 2022).

The second aim of our work was to evaluate how the historically-calibrated model influences long-term projections (Sect. 2.4.3). Using the best-ranked parameters, and those from the ad-hoc tuning, we ran forecast coupled simulations from 2013 to 2100 under two different climate forcing scenarios (FORE_*), giving a total of four long-term simulations.

All details for the hindcast ensemble and scoring, along with the forecast simulation design, are provided in the sections below and summarised in Table 1 and Fig. 3.

2.4.1 Ocean spin-up

Before running the hindcast ensemble, the ocean model was spun up with fixed ice-shelf cavities in two stages (SPIN_CTR and SPIN_VAR_CTR). In both stages and all CTR simulations, the surface forcing was derived from a six-hourly climatology of the 2000–2010 ERA5 atmospheric reanalysis, hereafter referred to as 'present-day' forcing. This period was selected to avoid spurious deep convection events known to occur after 2010 (Naughten et al., 2022), and provides a representative atmospheric state while suppressing interannual variability that could bias parameter optimization toward extreme or atypical events. A six-hourly rather than monthly averaging was chosen to preserve synoptic-scale variability, maintaining realistic short-term fluctuations in surface forcing and eliminating the need to retune MITgcm parameters to reproduce realistic water-mass distributions and sea-ice dynamics. While a repeating climatology was used, tests using the full 2000–2010 ERA5 time series (not

https://doi.org/10.5194/egusphere-2026-931
Preprint. Discussion started: 9 March 2026

Table 1. Summary of model simulations for the ocean spin-up (SPIN), hindcast ensemble (HIND) and forecast (FORE) stages. Two calibration approaches were used: transient-coupled (TR) snd static-melt (ST). The two forcing scenarios are present-day ERA5 climatology (CTR) and future RCP8.5 (WRM). A graphical representation of the experiment setup is shown in Fig. 3.

Experiment	Model	Time	Runs	Melt-rate parameters		
				C_d	γ_{T0}	H_{Trans}
					[m s^{-1}]	[m]
				($\times 10^{-3}$)	($\times 10^{-4}$)	
SPIN_CTR	MITgcm	18 yrs	1	8	N/A	0
SPIN_VAR_CTR	MITgcm	5 yrs	68	[1, 4, 8, 12]	[1, 2, 4, 8]	0:50:200
HIND_CTR	Úa-MITgcm	2013 – 2017	68	[1, 4, 8, 12]	[1, 2, 4, 8]	0:50:200
FORE_TR_CTR	Úa-MITgcm	2013 – 2100	1	8	8	50
FORE_ST_CTR	Úa-MITgcm	2013 – 2100	1	4	N/A	0
SPIN_TR_WRM	MITgcm	1990 – 2013	1	8	8	50
SPIN_ST_WRM	MITgcm	1990 – 2013	1	4	N/A	0
FORE_TR_WRM	Úa-MITgcm	2013 – 2100	1	8	8	50
FORE_ST_WRM	Úa-MITgcm	2013 – 2100	1	4	N/A	0

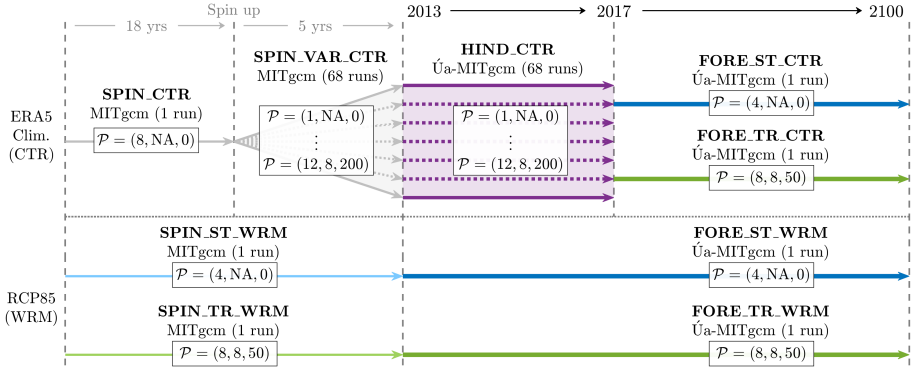

Figure 3. Schematic of the experiment setup showing the MITgcm spin ups (SPIN), followed by the coupled Úa-MITgcm simulations in the hindcast ensemble (HIND) and forecast (FORE) stages. The MITgcm simulations use the melt-rate parameter values obtained via the transient-coupled (TR) and static-melt (ST) calibration methods. The two forcing scenarios are: present-day ERA5 climatology (CTR) and future RCP8.5 (WRM). A summary of these model simulations is given in Table 1.

shown) yielded a comparable ice-sheet response, indicating that the ice sheet is broadly insensitive to interannual variability and justifying the use of the climatology for model calibration.

In the first spin-up stage, the model was initialized with temperature and salinity fields from a January climatology derived from World Ocean Atlas 2018 (WOA18), and extrapolated backwards into the cavities. Initial velocities were set to zero,

https://doi.org/10.5194/egusphere-2026-931
Preprint. Discussion started: 9 March 2026

while sea ice area, thickness, and snow thickness were initialized using the Biogeochemical Southern Ocean State Estimate, iteration 122 (B-SOSE). Open boundary conditions were prescribed using repeating monthly climatologies from WOA18 for temperature and salinity, and from B-SOSE for all other fields including ocean and sea ice velocities. Iceberg meltwater was applied as in Naughten et al. (2022). The model was then run for 18 years (SPIN_CTR) using a single set of melt-rate parameters ($C_d = 8 \times 10^{-3}$, γ_{T0} =N/A, $H_{\mathrm{Trans}} = 0$ m), after which MITgcm reached a quasi-steady state with no residual effects from the initial conditions.

In the second stage, the model was run for an additional five years (SPIN_VAR_CTR) in a suite of simulations with varying combinations of melt-rate parameter values (Table 1 and Fig. 3). The ranges selected for C_d and γ_{T0} were broad enough to encompass values used in previous studies (e.g., Jenkins et al., 2010; Naughten et al., 2022; Bett et al., 2024), while H_{Trans} is a new parameter introduced in this work. In total, 68 simulations were run, each with a unique parameter combination. With cavities held fixed, five years was sufficient for the ocean to adjust to the updated melt-rate parameters and the system to reach a new quasi-steady state, due to the relatively short residence time of the continental shelf in this region.

2.4.2 Hindcast ensemble and model calibration

Following the MITgcm spin-up with fixed cavities and varied melt-rate parameters, the ocean model was coupled with the ice-sheet model for the hindcast calibration stage (HIND_CTR), using the same climatological surface forcing as in the spin-up. An ensemble of 68 coupled hindcast simulations was run from the 2013 ice-sheet geometry to 2017. This period is long enough to capture reliable measurements of ice-sheet change and allow the ice sheet to respond dynamically to basal melting, while remaining computationally manageable.

We used this ensemble of hindcast simulations to calibrate the coupled model by identifying an optimal set of melt-rate parameters. Calibration was performed by computing a normalized likelihood score for each simulation, which quantifies the agreement between model output and observations relative to their uncertainties. This approach enables comparison across multiple observational datasets, including ice dynamical changes and melt rates, and combines these comparisons into a single overall score. Critically, we use spatial comparisons of modelled quantities rather than integrated metrics, such as volume above floatation or total melt. This ensures a better match with observed patterns of melting and thinning at the start of our coupled simulations, improving the reliability of long-term projections. The likelihood scoring approach allows the coupled model to be calibrated against the most up-to-date observations of ice-sheet changes, which has not been done previously. Likelihood-based metrics are widely used in model ensembles because they link prior information to posterior distributions and provide a formal means of quantifying parameter uncertainty (Nias et al., 2019; Coulon et al., 2024). In this study, the likelihood score was used to rank the 68 coupled simulations.

The likelihood score for all coupled simulations ($j = 1, \ldots, 68$), each of which used a set of unique melt-rate parameter values ($\mathcal{P}_j$), given observational dataset O_i was calculated as

$$\mathcal{L}_{i,j} \equiv \mathcal{L}\left(\mathcal{P}_j, O_i\right) = \exp\left[-\frac{1}{2\mathcal{A}} \int_{\mathcal{A}} \frac{\left(M_i(\mathcal{P}_j, \boldsymbol{x}) - O_i(\boldsymbol{x})\right)^2}{\left(\sigma_i^{\mathrm{mod}}(\boldsymbol{x})\right)^2 + \left(\sigma_i^{\mathrm{obs}}(\boldsymbol{x})\right)^2} d\boldsymbol{x}\right], \tag{5}$$

https://doi.org/10.5194/egusphere-2026-931
Preprint. Discussion started: 9 March 2026

Table 2. List of observational datasets that are used in the likelihood calculation.

Observation type	Errors	Source	Source date
Total change in ice thickness	From dataset	ITS_LIVE (Nilsson et al., 2022)	July 2013–July 2017
Total change in ice speed	From dataset	MEaSUREs (Mouginot et al., 2017a)	July 2013–July 2017
Time-average basal melt rates	Uniform 5 m yr^{-1}	Gourmelen et al. (2025)	2010–2021

where $\{O_i(\boldsymbol{x})\}_{i=1}^{N}$ are N independent observational datasets, such as melt rates and ice speed changes, and $M_i(\mathcal{P}_j, \boldsymbol{x})$ are the corresponding modelled spatial fields for parameter values $\mathcal{P}$. In the denominator, $\sigma_i^{\mathrm{mod}}(\boldsymbol{x})$ and $\sigma_i^{\mathrm{obs}}(\boldsymbol{x})$ are the model and observational uncertainties. This calculation was performed over the three major basins only (see Sect. 5.3) and there was a finite-element integration over this area ($\mathcal{A}$) to ensure different sized mesh triangles did not contribute equally to the overall score.

After the scores were calculated for each observation, they were normalized using the sum over all simulations:

$$\mathcal{L}_{i,j}^{\mathrm{Norm}} = \frac{\mathcal{L}_{i,j}}{\sum_j \mathcal{L}_{i,j}}. \tag{6}$$

The final likelihood score for each coupled model simulation, taking into account all observations, was given by the product of the individual normalized scores:

$$\mathcal{L}_j = \prod_{i=1}^{N} \mathcal{L}_{i,j}^{\mathrm{Norm}}. \tag{7}$$

As previously mentioned, melt-rate parameters in stand-alone ocean models or coupled ice sheet-ocean models are typically tuned using only a single set of melt-rate observations, i.e., $N = 1$ in Eq. (5) and Eq. (7). This approach ignores the ice sheet response, so the solution is to augment the likelihood with additional terms for spatial patterns of ice speed changes and ice thickness changes. To calibrate our model we used $N = 3$ individual data sources and these are listed in Table 2, with their spatial fields shown in Fig. 5.

The likelihood calculation accounts for uncertainties associated with both the observations and the model. For observed ice speed and thickness changes, we use the error estimates provided with the observational datasets (Table 2). However, satellite-derived melt-rate uncertainties reflect errors in elevation change and surface processes, such as surface mass balance and firn air content, rather than basal melt itself. This can lead to unrealistically small error estimates that disproportionately affect the ranking of simulations. To avoid this, we adopt a spatially-uniform error of 5 m yr^{-1} for the melt dataset. We also tested using the Úa diagnostic melt rate in place of the satellite-derived estimates (not shown), since this is what the ice-sheet model requires to reproduce observed thickness changes (Appendix B). This substitution yielded a similar ranking of simulations, with the highest-scoring parameters associated with the modified parameterization that concentrated melt near the grounding line.

In addition to observational uncertainty, the likelihood calculation incorporates uncertainty arising from model error. Because the coupled model is not a perfect representation of the real world, it is subject to structural uncertainties whose impacts on

https://doi.org/10.5194/egusphere-2026-931
Preprint. Discussion started: 9 March 2026

the modelled results are difficult to quantify. Such uncertainties may arise from missing or unknown model physics, or under-representation of the parameter space, and typically require expert judgement when scoring ensembles (Ritz et al., 2015). We tested different choices of model error, ensuring a reasonable spread across ensemble members rather than clustering around a small subset of simulations (not shown). This sensitivity analysis showed that the relative ranking of simulations was robust to the assumed error magnitudes. Given this robustness, and to avoid making additional assumptions about the form or magnitude of model errors, we adopt for simplicity a perfect-model assumption with zero errors ($\sigma_{i,j}^{\mathrm{mod}}(\boldsymbol{x}) = 0$ in Eq. 5).

2.4.3 Forecast simulations

The aim of these century-scale simulations was to quantify how calibration strategies influence long-term projections. We compared our new fully coupled calibration approach, which uses a modified melt-rate parameterization, transient ice-shelf geometry, and multiple observational constraints (melt rates, changes in ice speed and thickness), with the common approach that employs static ice-shelf geometry and melt-rate observations alone, using the default melt-rate parameterization. These two calibrations are hereafter referred to as Transient-Coupled (TR) and Static-Melt (ST).

For both calibration methods, we selected the top-ranked set of melt-rate parameters and ran simulations to 2100 under two forcing scenarios: (1) the six-hourly ERA5 climatology from 2000–2010 used in the ensemble simulations, representing present-day conditions; and (2) RCP8.5 surface forcing and transient boundary conditions from a single Community Earth System Model (CESM1) ensemble member, as described in Naughten et al. (2023). These simulations are referred to as FORE_*_CTR and FORE_*_WRM, respectively (Table 1 and Fig. 3). While we do not investigate sensitivity to surface forcing across different Earth System models or scenarios here, this remains an important topic for future work (Sect. 5.1).

The FORE_*_CTR simulations used the same MITgcm spin-up as the ensemble (SPIN_CTR), followed by the five-year adjustment period (SPIN_VAR_CTR) with updated melt-rate parameters and fixed ice-shelf cavities. In contrast, the FORE_*_WRM simulations used independent spin-ups tailored to the specific forcing (SPIN_*_WRM). For all four FORE_* simulations, ice-ocean coupling was initiated in 2013 and continued through 2100.

3 Coupled model calibration results

All 68 coupled model simulations, each defined by a unique combination of tunable melt parameters, $\mathcal{P} = (C_d, \gamma_{T0}, H_{\mathrm{Trans}})$, were ranked according to their agreement with spatial observations of ice-shelf melt rates, and observed changes in ice speed and thickness. The resulting likelihood scores (Eq. 5) are shown in Fig. 4, where lighter colours (yellow) indicate parameter combinations that best match the observations and darker colours (purple) denote lower-scoring simulations.

The five panels in Fig. 4 correspond to different transition-thickness constants (H_{Trans}). Within each panel, drag coefficients (C_d) and turbulent exchange velocities (γ_{T0}) vary along the x- and y-axes, respectively. For $H_{\mathrm{Trans}} = 0$ m (first panel), this corresponds to the default melt parameterization, where MITgcm simulations produced only velocity-dependent melt-rates, so the γ_{T0} parameter is not applicable. A spatial comparison between model results and observations for the two simulations outlined by the green and dashed blue lines is provided in Fig. 5.

https://doi.org/10.5194/egusphere-2026-931
Preprint. Discussion started: 9 March 2026

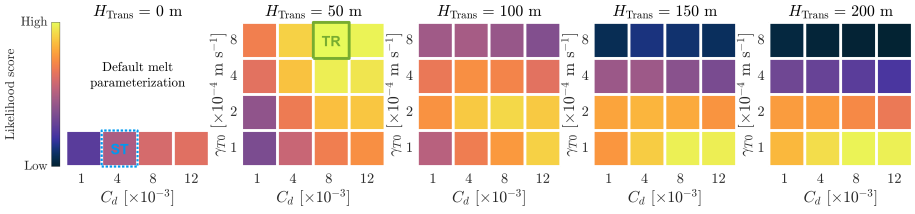

Figure 4. Likelihood scores (Eq. 5) for the 68 coupled ice sheet-ocean model simulations using all observational metrics (Table 2). The two boxes outlined in colour indicate the highest scoring simulations for the transient-coupled calibration method (TR, green-solid) and a static-melt calibration (ST, blue-dashed). Spatial maps for these two simulation are shown in Fig. 5 and these were selected to run to 2100 with present-day ERA5 (CTR) and future RCP8.5 (WRM) forcing.

3.1 Transient-coupled calibration

3.1.1 Highest-scoring parameters

The highest-scoring simulations over the hindcast period all used the modified melt parameterization, though not all simulations using this parameterization achieved high scores (Fig. 4). Compared to the default parameterization cases, these top-performing simulations produced elevated melt rates near the grounding line of the fast-flowing glaciers.

Within the set of high-scoring simulations, different parameter combinations produce better agreement with different observational metrics (Figs. B1–B3). Some combinations produce a good match with observed melt rates (e.g., $\mathcal{P} = (8, 1, 150)$, $\mathcal{P} = (8, 1, 200)$), whilst others produce better agreement with speed changes (e.g., $\mathcal{P} = (8, 8, 50)$, $\mathcal{P} = (12, 8, 50)$). This reflects the fact that the likelihood score represents a compromise across three metrics (melt rate, ice speed change, and thickness change) and three basins with distinct dynamics.

The diagonal band of lighter colours across Fig. 4 indicates the following: (1) simulations with velocity-independent melting confined to a thinner water column ($H_{\text{Trans}} = 50$ m) require either higher drag coefficients, which elevate melt rates across the entire ice shelf, or higher turbulent exchange velocities, which enhance melt locally, or a combination of both to achieve high scores; and (2) in high-scoring simulations where velocity-independent melt is applied across thicker water-column regions ($H_{\text{Trans}} \geq 150$ m), conversely the larger area of high melt requires lower exchange velocities ($\gamma_{T0} \leq 2 \times 10^{-4}$ m s^{-1}).

The highest-ranked set of parameter values was $C_d = 8 \times 10^{-3}$, $\gamma_{T0} = 8 \times 10^{-4}$ m s^{-1} and $H_{\text{Trans}} = 50$ m (green outline in Fig. 4). This optimal configuration reproduces observed melt rates and upstream thinning near the grounding line (Fig. 5, second column). Observed speed changes over the hindcast period are small (10s m yr^{-1}) relative to the observed mean flow speed (1000s m s^{-1}); the modelled speed change is slightly lower than observations, particularly for PIG. Some of this bias is likely attributable to ice damage and calving processes (Lhermitte et al., 2020; Joughin et al., 2021), which are not represented in the ice-sheet model. Importantly, these differences are within the uncertainty of the velocity measurements and reflect the regional optimization of the parameter set rather than a systematic error. Despite this, this configuration provides the best

https://doi.org/10.5194/egusphere-2026-931
Preprint. Discussion started: 9 March 2026

overall agreement with the available observations and is therefore selected for the transient-coupled calibration (TR). It is subsequently compared with a melt-only calibration in the forecast simulations (Sect. 4).

3.1.2 Lowest-scoring parameters

Among the 68 simulations, some of the lowest scores are associated with parameter combinations that produce low melting near the grounding line (Fig. 4, Fig. 5c). These correspond to $H_{\mathrm{Trans}} \leq 50$ m, $C_d \leq 4 \times 10^{-3}$ and $\gamma_{T0} \leq 2 \times 10^{-4}$ m s^{-1}, and include the four simulations that use the default melt-rate parameterization with different drag coefficients ($H_{\mathrm{Trans}} = 0$ m). Over the four-year coupled hindcast period, these low-scoring simulations exhibit little to no thinning immediately upstream of the grounding line and even show localized thickening of a few meters, in clear contrast to the observed changes. This leads to widespread glacier slowdown of up to 250 m yr^{-1} and grounding-line advance, most notably along the main trunk of PIG. Given the differences in deep melt rates between these low-scoring simulations and the Úa diagnostic melt rates (Fig. 2b,c,d), it is not surprising that there is an initial shock when the models are coupled together.

At the opposite extreme, simulations that use the modified melt parameterization with values that yield the highest melt in the vicinity of the grounding line ($H_{\mathrm{Trans}} \geq 150$ m and $\gamma_{T0} = 4 \times 10^{-4}$ m s^{-1}), produce excessive upstream thinning, overestimated speedup, and melt rates that exceed both observations and from modelled mass conservation (Fig. 2f).

3.2 Melt-only calibration

The results presented above are based on calibration using three different observational datasets. However, the analysis can be repeated using fewer observational constraints and different modelling approaches. When using only melt-rate observations in the calibration (while maintaining a transient ice-shelf geometry), the highest-scoring simulations shift towards those with velocity-independent melt over a wider region but lower γ_{T0} values (i.e., reduced turbulent exchange velocities and therefore lower melt rates) (Fig. B3). However, these same simulations are not the highest scoring when evaluated against changes in ice speed (Fig. B2).

To compare with the common practice in the literature, we also identified the highest-scoring simulation among those using only the *default* melt-rate parameterization with a *static* ice-shelf geometry. This simulation has a drag coefficient of $C_d = 4 \times 10^{-3}$ with γ_{T0} =N/A and $H_{\mathrm{Trans}} = 0$ m, as these parameters are not part of the default parameterization (dashed blue outline in Fig. 4 and third column in Fig. 5). When evaluated against all observational metrics using a transient geometry, this simulation ranks among the poorest performers. Nevertheless, because this represents the top-ranked parameter set following the most common calibration approach in the literature, we extend this simulation to 2100 and compare it with the transient-coupled calibration in Sect. 4.

Differences in data coverage within a given observation type also influence calibration outcomes. For instance, the limited availability of melt-rate estimates at the deep grounding lines in the dataset of Paolo et al. (2023) results in lower optimal melt parameter values than those obtained using Gourmelen et al. (2025) (not shown). Moreover, calibrating parameters for individual ice shelves instead of the regional domain can alter the choice of optimal parameter values, regardless of whether using a single dataset or a combination of all metrics (Figs. B1–B4). Although this has implications for future regional studies,

https://doi.org/10.5194/egusphere-2026-931
Preprint. Discussion started: 9 March 2026

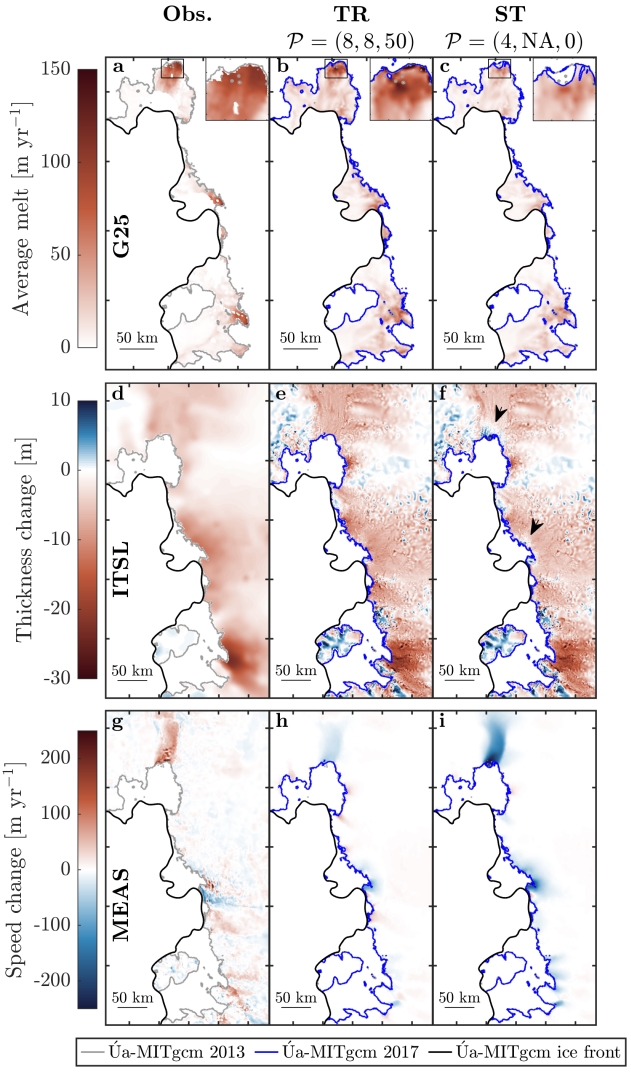

Figure 5. Observed and modelled spatial fields for the three metrics used in the likelihood calculation: average basal melt rate (**a–c**), total change in ice thickness (**d–f**) and total change in ice speed (**g–i**). The first column shows observations: G25 (Gourmelen et al., 2025), ITS (Nilsson et al., 2022), MEAS (Mouginot et al., 2017a). The second column shows the best-scoring parameters in the fully coupled transient calibration (TR), which uses melt rates and changes in ice speed and thickness. The third column shows the highest-scoring parameters in the static-melt calibration (ST). Inset panels in the first row show a zoom of the Pine Island main grounding line region. Small black arrows in **f** highlight regions of no thinning, in contrast to observations. The modelled 2013 and 2017 grounding lines at the start and end of the hindcast period for each simulation are shown as thin grey and blue lines, respectively, and the fixed ice front is shown as a black line.

https://doi.org/10.5194/egusphere-2026-931
Preprint. Discussion started: 9 March 2026

we do not explore the sensitivity of long-term projections to individual basin calibrations or different data products for each metric in detail here.

3.3 Implications of different calibration approaches

Tuning melt-rate parameters in an ocean model is a critical step in predicting future sea-level contribution. However, our hindcast simulations demonstrate that the calibration approach and which observations are used can affect the optimal parameter values. Typically, tuning is done using depth-binned or spatially-integrated values of basal melt for a static ice-sheet geometry. This approach has two key limitations. First, spatial-integration does not provide information about the distribution of melt, which we show matters for reproducing ice dynamics. Second, assuming a static geometry ignores geometric feedbacks that begin as soon as ice shelves thin through basal melting, and this might not represent future cavity conditions. Furthermore, satellite-derived melt-rate estimates are particularly uncertain or missing near the grounding line, which may limit their ability to constrain grounding-line dynamics when used alone. This is evident in our low-scoring coupled model simulations, where low grounding-line melt rates cause upstream thickening and slowdown, in contrast to observations (Figs. 4–5).

The modified melt-rate parameterization compensates for low vertical and horizontal resolution in the ocean model by generating enhanced melt near the grounding line, compared to the default parameterization. This allows a wider range of model behaviour to be captured and compared against observations, facilitating the selection of optimal parameters.

The diagonal band of high-scoring simulations in Fig. 4 demonstrates equifinality: multiple combinations of melt-rate parameters produce similarly good agreement with observations. This arises because the parameters exhibit trade-offs with one another. For example, a simulation with velocity-independent melt confined to a thin water column (low H_{Trans}) can achieve similar overall performance to one with velocity-independent melt over a thicker region (high H_{Trans}), provided the turbulent exchange velocity (γ_{T0}) or drag coefficient (C_d) is adjusted accordingly. The key requirement is that higher melt rates are concentrated near the grounding line and this can be achieved through different combinations of the three parameters.

Figure 6 shows the cumulative sea-level contribution from all coupled simulations compared with modern-day observations. The inset panels indicate that, by the end of the hindcast period, the Amundsen Sea Sector contributes between 1 and 2 mm to sea-level rise, consistent with observations. For each of the three major basins, the mass loss and rates of mass loss in almost all coupled simulations fall within the observational error bars. However, this does not mean that all parameter combinations are equally valid.

The 2013–2017 hindcast period is relatively short, and calibration based solely on integrated metrics such as volume above flotation over this timescale would provide limited constraint on model parameters (as done by Coulon et al., 2024). This limitation is exacerbated by observational uncertainties of 1 mm in integrated mass loss stemming in part from uncertainties in surface mass balance, which we keep fixed in our simulations. In contrast, our approach uses spatially-resolved observations of melt rates, ice speed changes, and thickness changes. This data-rich approach provides much stronger constraints over short timescales, allowing us to distinguish between parameter combinations that produce similar integrated mass loss but different spatial patterns of ice-ocean interaction. The likelihood-based calibration reveals a clear narrowing from the broad, uninformed

https://doi.org/10.5194/egusphere-2026-931
Preprint. Discussion started: 9 March 2026

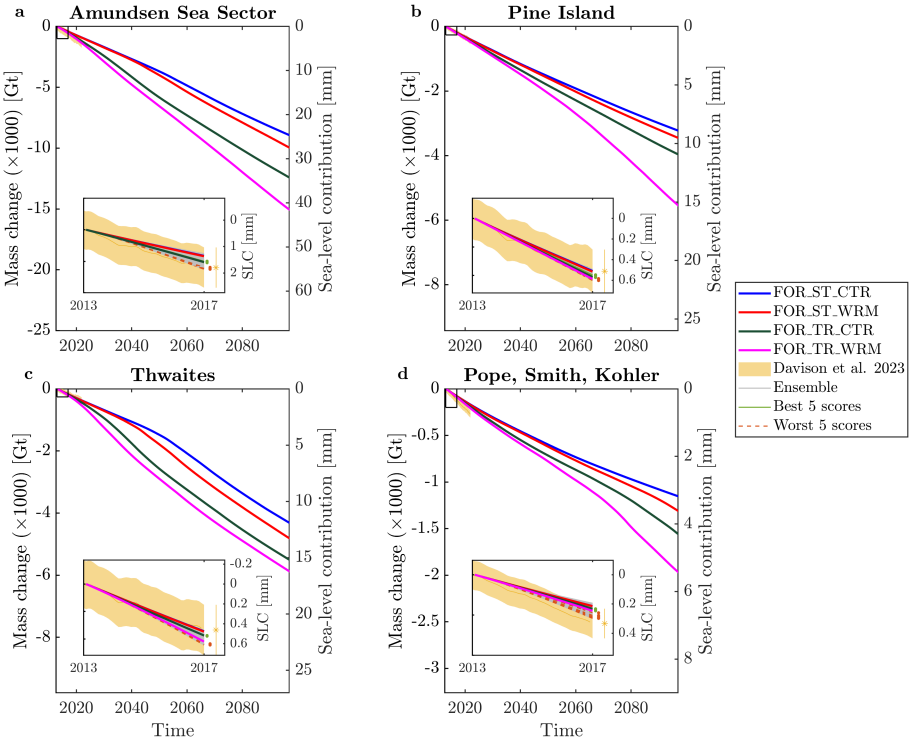

Figure 6. Change in volume above floatation (converted to mass, Gt) and the corresponding cumulative sea-level contribution for all coupled model simulations for the whole Amundsen Sea domain and the three major basins. The basin definitions are shown in Fig. 1a. In the inset of each panel, all simulations are compared against observations from Davison et al. (2023b) for the hindcast period (2013–2017). Also highlighted are the best (solid green) and worst (dashed orange) five scoring simulations. Dots are shown at the end to illustrate the range of modelled and observed sea-level contribution values in 2017.

prior parameter distribution to a well-localized posterior, demonstrating that spatial patterns provide powerful constraints even over relatively short periods.

Having identified optimal parameter sets through hindcast calibration, we extended these simulations to 2100 to assess the impact of calibration methods on projected sea-level contribution.

4 Historically-calibrated forecast simulations

Building on the hindcast evaluation, we assessed the sensitivity of the ice-sheet's long-term response to different calibration approaches by running two sets of melt-rate parameters to 2100 under two climate scenarios (Figs. 6–7). A six-hourly ERA5 climatology forcing, previously used in the hindcast ensemble, was applied for a present-day control run (CTR), while an RCP8.5 surface forcing was used for a future warm scenario (WRM).

https://doi.org/10.5194/egusphere-2026-931
Preprint. Discussion started: 9 March 2026

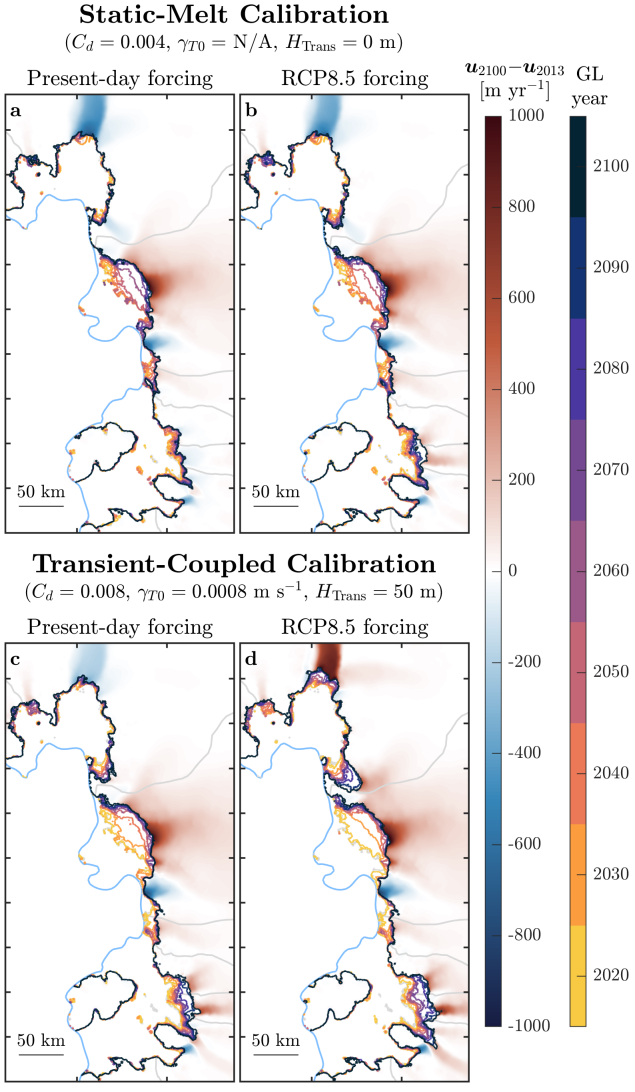

Figure 7. Evolution of the grounding line overlaid on the total change in speed for the four forecast simulations. The difference in speed is between the start of the coupling in 2013 and 2100 and the grounding line is shown for every 10 years.

The first parameter set (FORE_TR_*: $C_d = 8 \times 10^{-3}$, $\gamma_{T0} = 8 \times 10^{-4}$ m s^{-1}, $H_{\text{Trans}} = 50$ m), hereafter TR, corresponds to our transient-coupled calibration. The second (FORE_ST_*: $C_d = 4 \times 10^{-3}$, γ_{T0} =N/A, $H_{\text{Trans}} = 0$ m), hereafter ST, represents the top-performing simulation when only melt rates were compared against a static geometry. As previously discussed, TR outperformed ST in reproducing observed changes in ice speed and thickness during the hindcast period.

The following sections present the results of the aforementioned forecast simulations firstly for the entire Amundsen Sea sector followed by a regional analysis. We examine the sea-level contribution (Fig. 6) and the evolution of grounding-line retreat and ice speed changes (Fig. 7).

https://doi.org/10.5194/egusphere-2026-931
Preprint. Discussion started: 9 March 2026

4.1 Amundsen Sea sector

For the entire Amundsen Sea sector, all coupled simulations remain within the observational errors of sea-level contribution over the hindcast period. However, the different trends in mass loss lead to contrasting projections over longer timescales (Fig. 6a). Over the first 25 years, the two simulations that were calibrated using the full transient-coupled approach (TR) show accelerated mass loss and fast retreat of most of the major glaciers (Fig. 7c,d). By 2100, these simulations produce the largest retreat and highest sea-level contributions, reaching 34.62 mm (TR_CTR) and 41.98 mm (TR_WRM). In contrast, the simulations that were calibrated using only melt rates and a static geometry show a delayed response, with an initial slowdown in mass loss and localized grounding-line advance, resulting in lower final sea-level contributions of 24.92 mm (ST_CTR) and 27.80 mm (ST_WRM). Despite being forced with present-day ocean conditions, the CTR simulations produce at least 24 mm of sea-level rise from the Amundsen Sea Sector, because the ice-sheet is initialized in a transient state that reflects observed present-day thinning rates and velocities.

At the basin-scale, all four forecast simulations show continuous mass loss, but loss rates vary by calibration approach and forcing scenario (Fig. 6b-d). Approximately 45 % of the domain-wide loss comes from the Thwaites Glacier basin (THG), 35 % from Pine Island Glacier (PIG), and 12 % from Pope, Smith and Kohler (PSK). The TR_WRM simulation produces the largest contribution to sea-level rise (∼15–16 mm) and the highest mass-loss rates (∼80 Gt yr^{-1}) in both PIG and THG. However, the timing differs between these basins. THG initially loses mass and retreats rapidly before grounding-line migration slows down, whereas PIG shows an accelerating trend in mass loss and retreat towards the end of simulation (Fig. 6b,c and Fig. 7d). For PSK, TR_WRM also produces the fastest mass loss (∼32 Gt yr^{-1} after 2070), contributing 5.5 mm to sea level by 2100.

The TR and ST experiments demonstrate the lasting impact that different calibration methods can have on sea-level projections. Although both calibration methods produce similar cumulative mass loss over the hindcast period, and integrated values agree with observations, their spatial differences in melt rates and grounded ice dynamics lead to contrasting long-term behaviour. For our model setup, this means that calibrating melt parameters using only observations of melt rates underestimates sea-level contribution by 14 mm for the RCP8.5 forcing, representing a 20–50 % increase in mass loss for the domain as a whole and individual basins. This is because the transient approach requires higher melt rates to reproduce observed patterns of thinning and speedup upstream. Using ice-dynamics observations in the calibration allows us to overcome the limitations of relying solely on satellite-derived melt rates, which can be highly uncertain or unavailable near the grounding line. Crucially, the difference in mass loss arising from the calibration approach (10–14 mm) exceeds the difference arising from the forcing scenario (3–7 mm). This highlights the important role that the calibration methodology plays in century-scale projections. Although the relative influence of external forcing may increase over longer timescales, projections to 2100 remain highly policy-relevant, and our results demonstrate that calibration uncertainty is a leading-order contributor to near-term sea-level projections.

https://doi.org/10.5194/egusphere-2026-931
Preprint. Discussion started: 9 March 2026

4.2 Regional mass loss

4.2.1 Pine Island Glacier

For the PIG basin, in all but the TR_WRM case, the rate of mass loss decreases throughout the simulations despite continuous mass loss, resulting in similar limited retreat, slowdown and sea-level contribution by 2100. In both ST simulations, there is an initial grounding-line advance along the central trunk which takes over a decade to reverse (Fig. 7a,b).

In contrast, TR_WRM exhibits increasing mass-loss rates resulting in a cumulative loss that diverges from the other cases after 2050 (Fig. 6b). This leads to extensive retreat along the main fast-flowing trunk and also the southwest tributary ('Piglet Glacier'), which is close to intersecting with the retreating THG (Fig. 7d). Peak rates of mass loss of $\sim$80 Gt yr^{-1} occur around 2087 after much of the retreat has happened, and the grounding line then comes to rest on a series of shallower bumps in the bed. By 2100, there has been a large speedup of 1000 m yr^{-1} upstream of the main grounding line, and a retreat of 20 km.

The contrasting behaviour of PIG reflects the different spatial patterns of basal melt produced by the calibration methods. The static-melt calibration underestimates melt near the grounding line, while the transient-coupled approach produces higher melt in this region, better capturing observed ice dynamics. The difference becomes more pronounced under RCP8.5 forcing, where PIG exhibits the strongest response of all glaciers in the domain. This behaviour change may be due to warmer waters on the continental shelf (Mathiot and Jourdain, 2023; Naughten et al., 2023) having direct access to the deep grounding line. However, without a full analysis of the ocean model output, which is beyond the scope of this paper, it is difficult to identify the exact processes responsible because of the ice-ocean feedbacks involved.

4.2.2 Thwaites Glacier

Across all simulations, THG contributes the most to sea-level rise, loses mass the quickest, and retreats the furthest and fastest. In the transient-coupled (TR) calibrations during the modern-day period, there are multiple instances of modelled grounding-line retreat that agree well with recent observations (Wild et al., 2022; Chartrand et al., 2024; Ross et al., 2025; Andersen et al., 2025). In contrast, retreat in the first 10 years of both ST simulations is too slow compared to observations, which is likely caused by the lack of thinning immediately upstream of the grounding line (Fig. 5f).

In all simulations, by 2100, there is a speedup of Eastern Thwaites, which propagates tens of kilometres upstream, and a 40 km retreat of its grounding line. Once retreat starts, there is a similar temporal evolution in mass-loss rate across simulations, which consists of three phases: (1) accelerated loss during retreat from the present-day position, (2) a brief period ($\sim$10 years) of nearly constant peak mass-loss rate ($\sim$65–85 Gt yr^{-1}) during the fastest retreat, and (3) decreasing mass-loss rates to $\sim$50 Gt yr^{-1} by 2100 once the grounding line has retreated 40 km. Although they show similar retreat patterns, differences in rates of retreat and mass loss over the first 20 to 40 years result in slightly different overall sea-level contributions, with an approximate eight-year delay due to forcing, and 20-year delay due to calibration method.

In all simulations, the Eastern ice-shelf pinning point is lost, but this occurs at different times. The timing in our model may differ from observations because we do not include evolving ice damage or calving, which is likely to impact ice shelf structural integrity, ice flow and grounding-line retreat (Wild et al., 2022; Surawy-Stepney et al., 2023; Wang et al., 2025). In

https://doi.org/10.5194/egusphere-2026-931
Preprint. Discussion started: 9 March 2026

all four simulations, following the ungrounding of the Eastern ice-shelf pinning point, there is an acceleration of mass loss to its peak value and a retreat of the main grounding line.

In Western Thwaites, all simulations show similar retreat extent, with the grounding line of the western Thwaites ice tongue reaching a small-amplitude sill in the deep bed ∼15 km upstream. However, the timing varies considerably, with TR_WRM experiencing the fastest retreat. In this simulation, once the western grounding line reaches the upstream sill, it remains there for 65 years despite ongoing thinning.

For THG, by 2100 there is substantial speedup and extensive retreat regardless of forcing scenario or calibration method, though TR simulations show faster retreat and higher mass loss than ST. This supports the hypothesis that melting beneath its unconfined ice shelf, while influencing the rate of change, has a limited impact on whether retreat occurs (Gudmundsson et al., 2023). Therefore, retreat is likely already committed regardless of ocean forcing. Once the grounding line retreats inland, an embayment starts to form, which likely provides buttressing of upstream ice and potentially contributes to the decrease in mass-loss rates across all simulations. In both TR simulations, the retreat takes between 25 and 30 years from the start of coupling in 2013, which suggests we may see more rapid change from THG in the coming decades. The similarity in THG behaviour across calibrations contrasts sharply with the divergent responses seen for PIG, highlighting how different glaciers respond differently to calibration uncertainties.

4.2.3 Pope, Smith, Kohler Glaciers

For the PSK basin, in all cases except ST_CTR, there are increases in the rate of mass loss towards the end of the simulations, after initial periods of deceleration (Fig. 6d). In contrast, ST_CTR experiences an overall decrease in the rate of mass loss throughout the entire simulation. During the modern-day period, the initial pattern of retreat for all glaciers in the TR simulations is consistent with observations, whereas retreat in ST is not fast enough (Milillo et al., 2022). By 2100, the transient-calibrated simulations produce higher sea-level contributions than the static-melt approach, with the differences larger under warm forcing.

In the three simulations with accelerated mass loss, this period coincides with faster retreat along the Pope and Smith glaciers (Fig. 7b,c,d), occurring at various times depending on calibration and forcing. By 2100, there is also an overall speedup of these glaciers and a 30–40 km retreat. In contrast, for ST_CTR, there is limited and gradual retreat across the glaciers, and an eventual slowdown (Fig. 7a).

Downstream of Kohler East, there is a substantial pinning point that is lost early in the simulations, which may contribute to the modelled speedup and retreat seen in all cases. In all simulations, Kohler West retreats only a few kilometres to a shallow sill and remains there until 2100, and the overall speed slows down.

The PSK glaciers show sensitivity to calibration method similar to PIG. The TR simulations produce higher melt rates near the grounding line and in the shear zone between Crosson and Dotson ice shelves, which are regions that have a high sensitivity to melt (Goldberg et al., 2019; Morlighem et al., 2021). This leads to a speedup and retreat of the glaciers flowing into the Crosson Ice Shelf (Pope, Smith, Kohler East). The ST simulations show minimal dynamic response in these regions under present-day forcing.

https://doi.org/10.5194/egusphere-2026-931
Preprint. Discussion started: 9 March 2026

4.2.4 Summary: Calibration method versus forcing scenario

The different behaviour due to calibration method is evident across the Amundsen Sea sector, though the magnitude of this difference varies by glacier. The spatial differences in melt patterns drive markedly different ice dynamics. Under present-day forcing with the static-melt calibration, low melt rates near the grounding line cause widespread slowdown and limited retreat across all glaciers except Thwaites. In contrast, the transient-coupled calibration generates higher melt rates near the grounding line, leading to speedup and retreat across most glaciers. Despite these contrasting behaviours, both calibrations show increased sea-level contribution across the sector, suggesting that the glaciers remain out of balance regardless of calibration method, though the magnitude and spatial pattern of imbalance differ substantially.

The contrasting response between PIG and THG is important for future regional studies. PIG shows strong sensitivity to calibration method, with TR_WRM producing substantially more retreat and mass loss than the ST simulations. In contrast, THG shows similar retreat patterns across all calibrations, and the 40 km retreat occurs within a few decades in the TR simulations regardless of forcing scenario. The pattern of modelled grounding-line retreat across all glaciers is broadly consistent with other coupled ice-ocean modelling studies of this region, though the timing and extent of retreat differs slightly depending on calibration and forcing (Goldberg and Holland, 2022; De Rydt and Naughten, 2024; Bett et al., 2024).

By incorporating observations of ice speed and thickness changes alongside melt rates, and by allowing the ice-shelf geometry to evolve during calibration, our transient-coupled approach captures spatial patterns of melting that are necessary for reproducing observed ice dynamics. The resulting projections differ from those produced using melt rates alone, and these differences exceed the impact from climate forcing scenarios. This suggests that reducing uncertainty in sea-level projections from West Antarctica requires not only improved climate models and forcing scenarios, but also improved methods for calibrating coupled ice-ocean models.

The combined run time for all spin-ups and 68 calibration simulations was approximately 317 days, while a single 90-year forecast simulation added another 53 days. Thus, calibration accounted for 85.6 % of the total 370-day run time. While this represents a significant upfront computational investment, it is a one-off process that establishes an optimised parameter set. Once calibrated, the model can be used for multiple future projections, ensuring that subsequent forecasts are both efficient and consistent with observational constraints.

5 Limitations and future work

The objectives of this study were to calibrate a coupled ice sheet-ocean model using combined measurements of ice-shelf melt rates and changes in ice speed and thickness, and then to provide century-scale projections of sea-level contribution under different climate scenarios. While our approach addresses key limitations in previous studies, there are several aspects that would benefit from consideration in future work.

https://doi.org/10.5194/egusphere-2026-931
Preprint. Discussion started: 9 March 2026

5.1 Ocean model

We introduced a modified melt-rate parameterization to address resolution limitations of the z-coordinate ocean model in capturing enhanced melting near grounding lines, consistent with observations. Although this formulation is heuristic rather than derived from first principles, it enables elevated melt rates in this critical region and broadens the parameter space available for calibration. Future work should aim to develop a more physically grounded representation of grounding-line processes that achieves similar performance without requiring prohibitively high resolution.

In the calibration, we used a discrete set of melt-rate parameter values (68 simulations for three parameters), chosen strategically for comparison with previous studies. While a more rigorous approach would randomly sample values across a wider range, we do not expect this to change our main conclusions. Furthermore, the results in Fig. 4 suggest a relatively linear relationship between parameter values and ice response, rather than any complex or non-linear dependencies, so additional simulations are not likely to provide additional information.

Our simulations extend to 2100 under present-day control and an extreme RCP8.5 forcing scenario, which was sufficient for evaluating the impact of calibration methods on long-term ice-sheet response. However, we only use a repeating ERA5 2000-2010 six-hourly climatology to represent present-day forcing and a single ensemble member from one earth system model for the warm scenario. Therefore, future work should further consider the uncertainties in sea-level rise related to ocean forcing and climate scenarios (Naughten et al., 2023; Seroussi et al., 2024).

5.2 Ice-sheet model

While we calibrated the basal melt-rate parameters in the ocean model using a comprehensive set of simulations and observations, we used a single set of ice-sheet model parameters, which may not represent the true optimal choice. Several ice-sheet parameters contribute highly to projection uncertainty, including the sliding law and its exponent, the flow-law exponent, and parameters in the inversion regularization process (Barnes and Gudmundsson, 2022; Getraer and Morlighem, 2025; Rosier et al., 2025). Ice speed and thickness changes are physically coupled through the ice-flow equations, and in a fully calibrated ice-sheet model, these dependencies mean that calibrating against either metric would produce the same optimal basal melt parameters. In our current results, calibrating against individual ice-dynamics metrics produces different likelihood scores and optimal melt parameters (Figs. B1–B2) because the ice-sheet model parameters themselves have not been historically calibrated.

The next iteration of this coupled-model calibration will explore a range of historically calibrated ice-dynamics parameters (De Rydt, 2026). This approach will enable fully consistent coupled ice-ocean projections that match historical satellite observations of basal melt, ice thickness, and ice speed. Importantly, by calibrating the ice-sheet model using ice-dynamics observations, the calibration of the ocean melt parameters would only require one type of these datasets along with melt observations. Furthermore, the stochastic framework will allow uncertainties from individual model parameters to be propagated to the projections, providing a clear attribution of uncertainty in future ice-ocean simulations.

https://doi.org/10.5194/egusphere-2026-931
Preprint. Discussion started: 9 March 2026

5.3 Likelihood calculation

The likelihood scores for each coupled simulation were calculated across the three major basins (Pine Island, Thwaites, and Pope-Smith-Kohler), rather than the whole domain, for the following reasons. These basins contain the fastest-flowing glaciers (Fig. 1a), which are experiencing the greatest mass loss in West Antarctica (Smith et al., 2020). Consequently, there is much more data available for model setup in these regions. The MITgcm configuration was tuned and validated using temperature and salinity measurements from the neighbouring oceanic regions of Pine Island Bay, Dotson Ice front, and Pine Island-Thwaites West Trough (Naughten et al., 2022). Additionally, initialization of the ice-sheet model was based on previous studies that were focussed entirely on these highly dynamic regions (Reed et al., 2024; De Rydt and Naughten, 2024). Therefore, ensemble likelihood scores were calculated using this region only. This ensured a balance between reproducing the observed mass loss across the ASE, while avoiding overfitting to individual glaciers which have their own sensitivities and optimal parameter values (Figs. B1–B4).

5.4 Hindcast ensemble

As mentioned previously (Sect. 2), the hindcast window of 2013–2017 was chosen because this period provides the most comprehensive data coverage for model initialization and comparison, while avoiding large velocity changes associated with damage and calving (Joughin et al., 2021; Sun and Gudmundsson, 2023), which are not represented in the model. Despite its limited duration, the calibration window is sufficiently long to constrain melt parameters using the spatial patterns of ice-dynamics change. Future work could examine how varying the start date and duration of the calibration window affects the results. Different initialization and hindcast periods would alter the transient state of the ice sheet and, consequently, the basal slipperiness and ice viscosity inferred through inversion. An advantage of our likelihood-based ranking approach is that it readily accommodates new observations as they become available, particularly improved estimates of transient melt rates and associated uncertainties.

Despite the limitations, our transient-coupled calibration approach represents a significant advance in capturing the complex interactions between ice dynamics and ocean melting. Our results demonstrate that calibrations using present-day melt estimates alone systematically underestimate ice-sheet response over the historical period. By incorporating ice dynamics constraints, this bias is removed entirely, resulting in more robust projections of future mass loss.

6 Conclusions

In this study we presented a new method for calibrating melt-rate parameters in coupled ice sheet-ocean models using remote sensing measurements of basal melt rates and changes in ice speed and thickness. Whereas previous calibrations have relied on melt estimates only and assumed static ice-shelf geometries, we have shown that including feedbacks between basal melting, evolving ice thickness, and cavity circulation in the calibration leads to a greatly improved representation of ice-sheet dynamics over the observational period. We show that the longer-term consequences of this improved calibration result in 14 mm addi-

https://doi.org/10.5194/egusphere-2026-931
Preprint. Discussion started: 9 March 2026

tional sea-level rise by 2100 under an RCP8.5 scenario. These coupled processes are critical to model accuracy, particularly in the rapidly changing Amundsen Sea sector.

To calibrate ocean-model melt parameters, we ran an ensemble of coupled simulations with varying parameter values in a modified melt parameterization. We compared modelled outputs against observed spatial patterns of ice-shelf melt rates and changes in ice speed and thickness between 2013 and 2017. With this approach, parameter combinations that enhanced melt in the vicinity of the grounding line produced the best match with observations of thinning and accelerating grounded ice while also constraining overall melt rates. In contrast, the common approach of tuning against only melt observations for a static geometry produced optimal values with low grounding-line melt, leading to coupling shocks and widespread glacier slowdown.

Using optimal parameters from the transient-coupled calibration, we projected century-scale mass loss under two climate scenarios and compared these against the static-melt approach. All simulations showed continuous mass loss and retreat of major glaciers by 2100, though at varying rates. Under RCP8.5, the transient calibration projected 42 mm of sea-level rise compared to 28 mm for the static-melt case: a 14 mm difference that exceeds the impact of changing the climate forcing alone. These findings highlight the critical role of multi-observational calibration in reducing parameter uncertainties and improving projection confidence.

Code and data availability. The individual model components are publicly available: Úa at https://zenodo.org/records/3706624 and MITgcm at https://github.com/MITgcm/MITgcm. The coupled model configuration Úa-MITgcm, along with all code and data necessary to reproduce the results and figures presented in this study, will be made available upon acceptance of the manuscript.

Appendix A: Úa Initialization

To initialize the ice-sheet model in an approximate present-day state, the following three-stage procedure was implemented. The first step was to use an inverse method with data assimilation to derive both spatially varying fields of ice-rate factor A and slipperiness C in the flow law and sliding law, respectively. This was done by minimizing the cost function $J = I + R$, where I is a misfit term and R is a Tikhonov regularization term. In this first initialization step, we ran a velocity-only inversion such that I is given as

$$I = \frac{1}{2\mathcal{A}} \int \left(\frac{u_{\mathrm{mod}} - u_{\mathrm{obs}}}{u_{\mathrm{err}}} \right)^2 + \left(\frac{v_{\mathrm{mod}} - v_{\mathrm{obs}}}{v_{\mathrm{err}}} \right)^2 d\boldsymbol{x}, \tag{A1}$$

where $u_{\mathrm{obs}}, v_{\mathrm{obs}}$ are observed MEaSUREs ice-surface velocities and $u_{\mathrm{err}}, v_{\mathrm{err}}$ are their corresponding measurement errors (Mouginot et al., 2017b; Rignot et al., 2017), while $\mathcal{A} = \int d\boldsymbol{x}$ is the full model domain area. The Tikhonov regularization term

https://doi.org/10.5194/egusphere-2026-931
Preprint. Discussion started: 9 March 2026

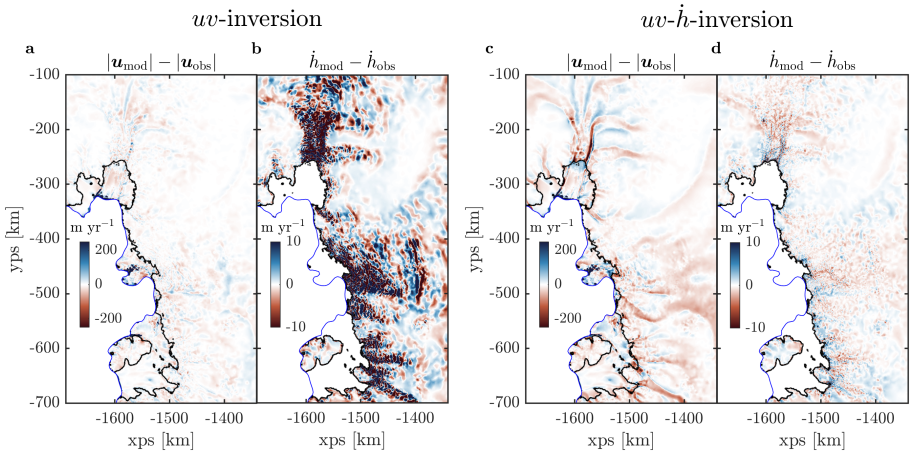

Figure A1. Difference between modelled and observed ice-surface speed (**a**, **c**) and thickness changes (**b**, **d**) for the velocity-only inversion (**a**, **b**) and for the velocity and thickness-change inversion following a five-year relaxation period (**c**, **d**). In (**b**) and (**d**), floating regions have been masked out, for illustration purposes only, due to large thickness changes resulting from no basal melting in the inversions.

ensures we do not overfit to the measurements and is given by

$$R = \frac{1}{2\mathcal{A}} \int \left[\gamma_{sA}^2 \left(\nabla \log_{10} \left(\frac{A}{\hat{A}} \right) \right)^2 + \gamma_{sC}^2 \left(\nabla \log_{10} \left(\frac{C}{\hat{C}} \right) \right)^2 + \gamma_{aA}^2 \left(\log_{10} \left(\frac{A}{\hat{A}} \right) \right)^2 + \gamma_{aC}^2 \left(\log_{10} \left(\frac{C}{\hat{C}} \right) \right)^2 \right] d\mathcal{A}, \tag{A2}$$

where $\hat{A}$ and $\hat{C}$ are prior estimates for A and C, and γ_{sA}, γ_{sC}, γ_{aA} and γ_{aC} are pre-multipliers that penalise deviation in local slope and amplitude of A and C fields from their priors. Following Reed et al. (2024) and De Rydt et al. (2021), the priors were chosen to be spatially uniform with $\hat{A} = 5 \times 10^{-9}$ yr^{-1} kPa^{-3}, corresponding to an ice temperature of -15 °C, and $\hat{C} = u_b \tau_b^{-m} = 1.46 \times 10^{-3}$ m yr^{-1} kPa^{-3}, with basal traction $\tau_b = 80$ kPa and velocity $u_b = 750$ m yr^{-1}, while the regularization pre-multipliers were set to $\gamma_{sA} = \gamma_{sC} = 25{,}000$ m and $\gamma_{aA} = \gamma_{aC} = 1$.

From this inversion, the modelled and observed surface speeds showed a good agreement, with a mean difference of 15.7 m yr^{-1} and standard deviation of 93.3 m yr^{-1} (Fig. A1a). However, because modelled ice-thickness change is left unconstrained, the inversion produces unrealistically large thickness changes along fast-flowing glaciers compared with observations, with a mean difference of 2.1 m yr^{-1} and a standard deviation of 24.1 m yr^{-1} (Fig. A1b).

To address any potential model shock due to the large changes in ice thickness, additional steps were taken in the initialization. Similar to previous studies, we ran the model with a transient relaxation period, using the modelled velocities from the first inversion, while keeping the ice thickness in floating regions fixed (De Rydt and Naughten, 2024; Rosier et al., 2025). The model was run for five years to allow upstream ice to equilibrate, while minimising deviations from the present-day geometry and preventing any grounding-line migration.

https://doi.org/10.5194/egusphere-2026-931
Preprint. Discussion started: 9 March 2026

Using the updated ice geometry after the relaxation period, a second inversion was performed with an additional constraint on ice thickness changes, such that the misfit term (Eq. A1) in the cost function becomes

$$I = \frac{1}{2\mathcal{A}} \int \left(\frac{u_{\mathrm{mod}} - u_{\mathrm{obs}}}{u_{\mathrm{err}}} \right)^2 + \left(\frac{v_{\mathrm{mod}} - v_{\mathrm{obs}}}{v_{\mathrm{err}}} \right)^2 + \left(\frac{\dot{h}_{\mathrm{mod}} - \dot{h}_{\mathrm{obs}}}{\dot{h}_{\mathrm{err}}} \right)^2 d\boldsymbol{x}, \tag{A3}$$

where $\dot{h}_{\mathrm{obs}}$ are observed thickness changes over a three-year window, centred on 2015.5, for grounded ice (Shepherd et al., 2019) and floating ice (Paolo et al., 2023). As in previous studies, thickness change errors were chosen to be spatially uniform with $\dot{h}_{\mathrm{err}} = 0.1$ m yr^{-1} for grounded regions and a larger error of $\dot{h}_{\mathrm{err}} = 100$ m yr^{-1} for floating areas, to account for uncertainty in basal melt rates (De Rydt and Naughten, 2024; Rosier et al., 2025). Including ice-thickness changes in the second inversion leads to much better agreement with observations: the mean difference is reduced to 0.5 m yr^{-1} and standard deviation to 1.2 m yr^{-1} (Fig. A1d). This improvement, however, comes at a slight cost to the modelled velocities, where the mean difference increases to 21.1 m yr^{-1} and standard deviation to 71.2 m yr^{-1}(Fig. A1c).

Appendix B: Úa diagnostic melt rate

Using the ice-sheet model Úa and combined observations of present-day velocities (u, v), surface mass balance (a_s) and rates of thickness change (dh/dt), we can estimate a diagnostic basal melt-rate field using mass conservation:

$$a_b = -\left(\frac{1}{\rho} \frac{\partial h}{\partial t} + \left(\frac{\partial (uh\rho_i)}{\partial x} + \frac{\partial (vh\rho_i)}{\partial y} \right) - a_s \right), \tag{B1}$$

where the x and y components of the ice flux are given by $q_x = uh\rho_i$ and $q_y = vh\rho_i$. By comparing this diagnostic melt rate against MITgcm-simulated melt, we can assess whether coupling the two models together will produce an initial shock, where a mismatch would likely cause the ice-sheet model to exhibit thickness changes that are inconsistent with present-day observations. For example, the melt rates from the default MITgcm melt parameterization with two different drag coefficients (Fig. 2c,d) both produce lower melt rates close to the Pine Island Glacier grounding line compared to the diagnostic melt rate, which when coupled with Úa leads to unrealistic ice-shelf grounding and the slowdown and thickening of grounded ice (Fig. 5).

Author contributions. BR and JDR conceptualised the study. BR performed all model simulations, subsequent analysis and wrote the manuscript. KAN provided the ocean model configuration, forcing and the latest version of Úa-MITgcm. DNG produced the modified melt parameterization. All authors reviewed and edited the manuscript.

Competing interests. JDR serves as a topical editor of The Cryosphere. There are no other competing interests.

Acknowledgements. BR and JDR were funded through a UK Research and Innovation (UKRI) Future Leaders Fellowship [grant number MR/W011816/1]. JDR was supported by the UK government's Horizon Europe funding Guarantee [grant number 10044471]. This research

https://doi.org/10.5194/egusphere-2026-931
Preprint. Discussion started: 9 March 2026

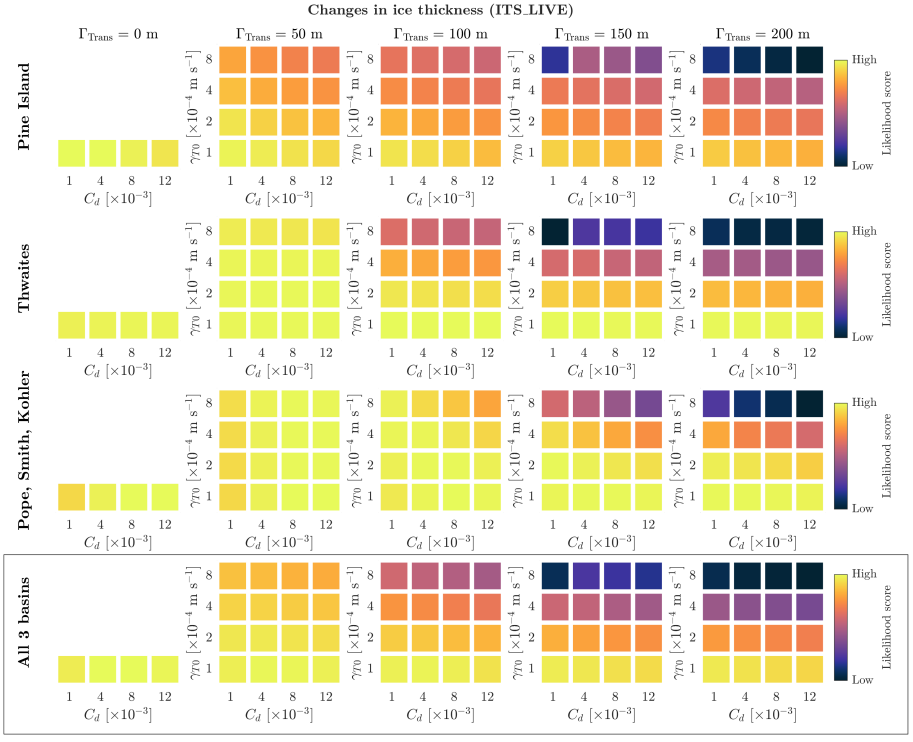

Figure B1. Likelihood scores for the 68 coupled ice-ocean model simulations when comparing only ice-thickness changes with observations from Nilsson et al. (2022). The top three rows show scores calculated over separate basins, whilst the bottom row is across all three key basins.

was also supported by Ocean Cryosphere Exchanges in ANtarctica: Impacts on Climate and the Earth system, OCEAN ICE, which is funded by the European Union, Horizon Europe Funding Programme for research and innovation under grant agreement Nr. 101060452, 10.3030/101060452. OCEAN ICE contribution number 50. KAN was supported by the TerraFIRMA project (grant number NE/W004895/1). DNG was supported by UKRI Natural Environment Research Council Grant UKRI1266.

https://doi.org/10.5194/egusphere-2026-931
Preprint. Discussion started: 9 March 2026

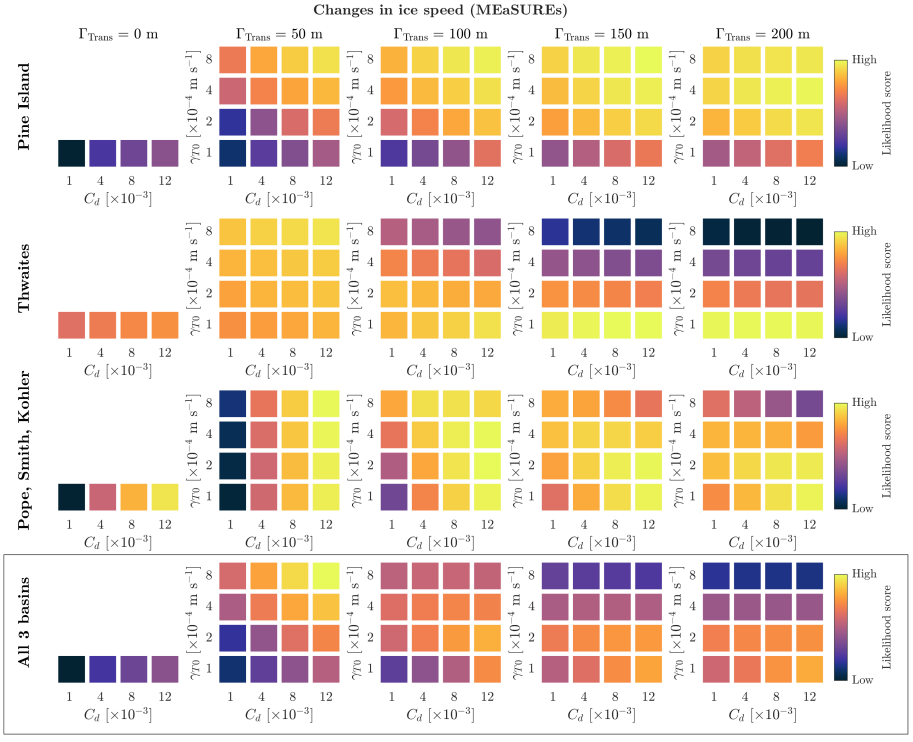

Figure B2. As in Fig. B1 but for ice-speed changes using observations from Mouginot et al. (2017a).

References

Andersen, J. K., Millan, R., Rignot, E., Scheuchl, B., Barré, J. B., and Bjørk, A. A.: Brief communication: Updated grounding line mapping in the Amundsen Sea Embayment, Antarctica, from 1-day repeat Sentinel-1 SAR data [Preprint], EGUsphere, 2025, 1–13, https://doi.org/10.5194/egusphere-2025-4471, 2025.

Barnes, J. M. and Gudmundsson, G. H.: The Predictive Power of Ice Sheet Models and the Regional Sensitivity of Ice Loss to Basal Sliding Parameterisations: A Case Study of Pine Island and Thwaites Glaciers, West Antarctica, The Cryosphere, 16, 4291–4304, https://doi.org/10.5194/tc-16-4291-2022, 2022.

Bett, D. T., Holland, P. R., Naveira Garabato, A. C., Jenkins, A., Dutrieux, P., Kimura, S., and Fleming, A.: The Impact of the Amundsen Sea Freshwater Balance on Ocean Melting of the West Antarctic Ice Sheet, Journal of Geophysical Research: Oceans, 125, e2020JC016 305, https://doi.org/10.1029/2020JC016305, 2020.

Bett, D. T., Bradley, A. T., Williams, C. R., Holland, P. R., Arthern, R. J., and Goldberg, D. N.: Coupled Ice–Ocean Interactions during Future Retreat of West Antarctic Ice Streams in the Amundsen Sea Sector, The Cryosphere, 18, 2653–2675, https://doi.org/10.5194/tc-18-2653-2024, 2024.

Burgard, C., Jourdain, N. C., Reese, R., Jenkins, A., and Mathiot, P.: An Assessment of Basal Melt Parameterisations for Antarctic Ice Shelves, The Cryosphere, 16, 4931–4975, https://doi.org/10.5194/tc-16-4931-2022, 2022.

https://doi.org/10.5194/egusphere-2026-931
Preprint. Discussion started: 9 March 2026

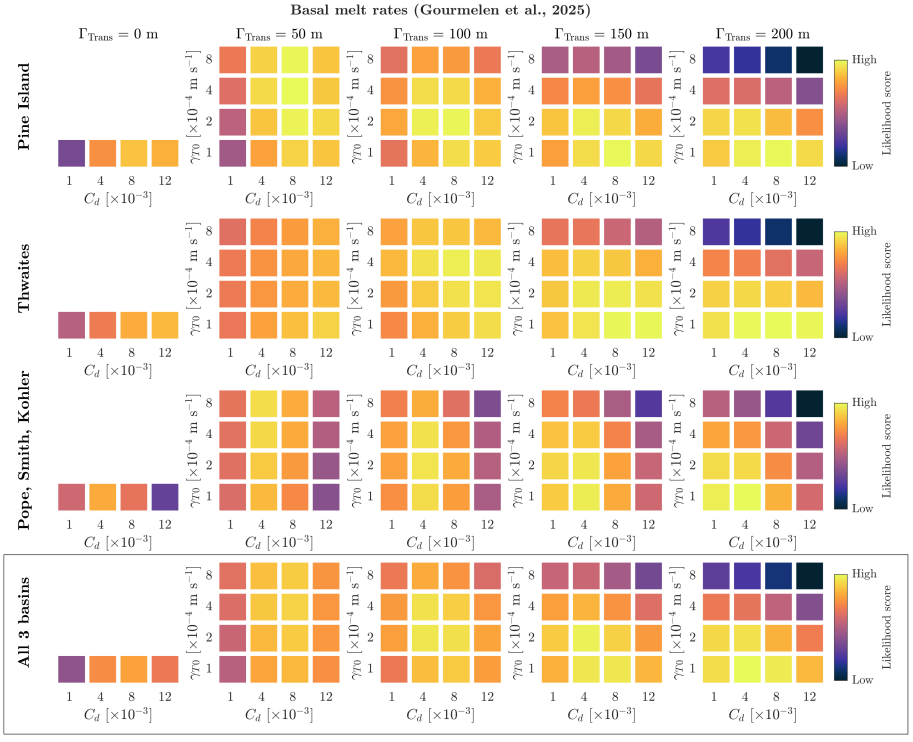

Figure B3. As in Fig. B1 but for basal melt rates with observations from Gourmelen et al. (2025).

Chartrand, A. M., Howat, I. M., Joughin, I. R., and Smith, B. E.: Thwaites Glacier Thins and Retreats Fastest Where Ice-Shelf Channels Intersect Its Grounding Zone, The Cryosphere, 18, 4971–4992, https://doi.org/10.5194/tc-18-4971-2024, 2024.

Coulon, V., Klose, A. K., Kittel, C., Edwards, T., Turner, F., Winkelmann, R., and Pattyn, F.: Disentangling the Drivers of Future Antarctic Ice Loss with a Historically Calibrated Ice-Sheet Model, The Cryosphere, 18, 653–681, https://doi.org/10.5194/tc-18-653-2024, 2024.

Dansereau, V., Heimbach, P., and Losch, M.: Simulation of Subice Shelf Melt Rates in a General Circulation Model: Velocity-dependent Transfer and the Role of Friction, Journal of Geophysical Research: Oceans, 119, 1765–1790, https://doi.org/10.1002/2013JC008846, 2014.

Davison, B. J., Hogg, A. E., Gourmelen, N., Jakob, L., Wuite, J., Nagler, T., Greene, C. A., Andreasen, J., and Engdahl, M. E.: Annual Mass Budget of Antarctic Ice Shelves from 1997 to 2021, Science Advances, 9, eadi0186, https://doi.org/10.1126/sciadv.adi0186, 2023a.

Davison, B. J., Hogg, A. E., Rigby, R., Veldhuijsen, S., van Wessem, J. M., van den Broeke, M. R., Holland, P. R., Selley, H. L., and Dutrieux, P.: Sea Level Rise from West Antarctic Mass Loss Significantly Modified by Large Snowfall Anomalies, Nature Communications, 14, 1479, https://doi.org/10.1038/s41467-023-36990-3, 2023b.

De Rydt, J.: Basal sliding and ice rheology in West Antarctica constrained by multi-epoch satellite observations., ESS Open Archive, https://doi.org/10.22541/essoar.176894749.90399034/v1, 2026.

De Rydt, J. and Naughten, K.: Geometric Amplification and Suppression of Ice-Shelf Basal Melt in West Antarctica, The Cryosphere, 18, 1863–1888, https://doi.org/10.5194/tc-18-1863-2024, 2024.

https://doi.org/10.5194/egusphere-2026-931
Preprint. Discussion started: 9 March 2026

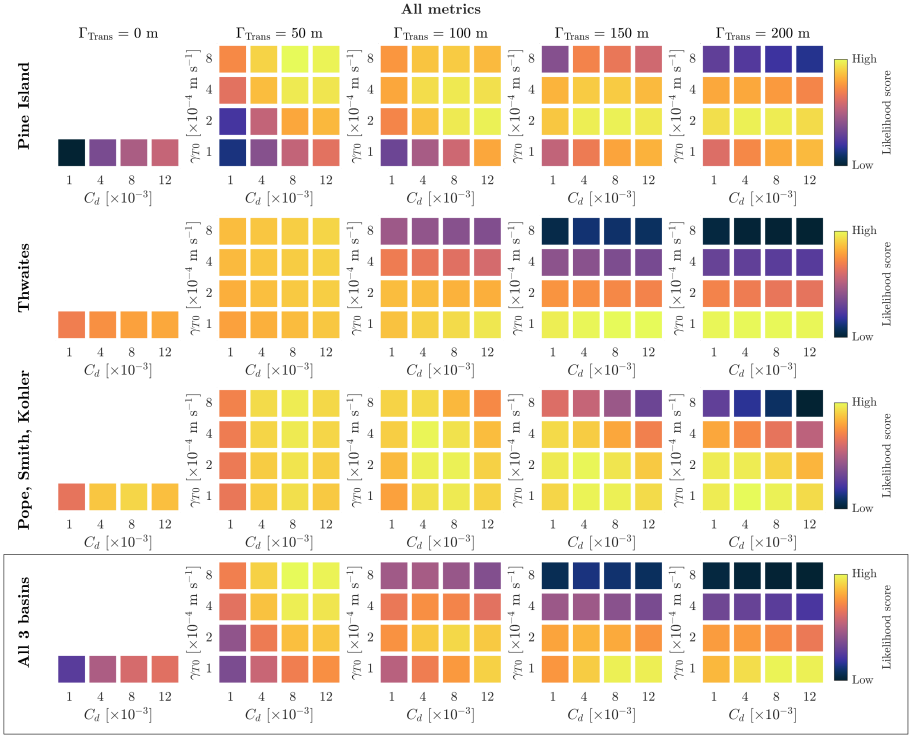

Figure B4. As in Fig. B1 but for all modelled metrics. The bottom row is the same as Fig. 4.

De Rydt, J., Holland, P. R., Dutrieux, P., and Jenkins, A.: Geometric and Oceanographic Controls on Melting beneath Pine Island Glacier, Journal of Geophysical Research: Oceans, 119, 2420–2438, https://doi.org/10.1002/2013JC009513, 2014.

De Rydt, J., Reese, R., Paolo, F. S., and Hilmar Gudmundsson, G.: Drivers of Pine Island Glacier Speed-up between 1996 and 2016, Cryosphere, 15, 113–132, https://doi.org/10.5194/tc-15-113-2021, 2021.

Dinh, A., Rignot, E., Mazloff, M., and Fenty, I.: Modeling Ocean Heat Transport to the Grounding Lines of Pine Island, Thwaites, Smith, and Kohler Glaciers, West Antarctica, Geophysical Research Letters, 51, e2024GL110 078, https://doi.org/10.1029/2024GL110078, 2024.

Donat-Magnin, M., Jourdain, N. C., Spence, P., Le Sommer, J., Gallée, H., and Durand, G.: Ice-Shelf Melt Response to Changing Winds and Glacier Dynamics in the Amundsen Sea Sector, Antarctica, Journal of Geophysical Research: Oceans, 122, 10 206–10 224, https://doi.org/10.1002/2017JC013059, 2017.

Dotto, T. S., Garabato, A. C., Bacon, S., Holland, P. R., Kimura, S., Firing, Y. L., Tsamados, M., Wåhlin, A. K., and Jenkins, A.: Wind-Driven Processes Controlling Oceanic Heat Delivery to the Amundsen Sea, Antarctica, Journal of Physical Oceanography, 49, 2829–2849, https://doi.org/10.1175/JPO-D-19-0064.1, 2019.

Dotto, T. S., Naveira Garabato, A. C., Wåhlin, A. K., Bacon, S., Holland, P. R., Kimura, S., Tsamados, M., Herraiz-Borreguero, L., Kalén, O., and Jenkins, A.: Control of the Oceanic Heat Content of the Getz-Dotson Trough, Antarctica, by the Amundsen Sea Low, Journal of Geophysical Research: Oceans, 125, e2020JC016 113, https://doi.org/10.1029/2020JC016113, 2020.

Dupont, T. K. and Alley, R. B.: Assessment of the Importance of Ice-Shelf Buttressing to Ice-Sheet Flow, Geophysical Research Letters, 32, L04 503, https://doi.org/10.1029/2004GL022024, 2005.

https://doi.org/10.5194/egusphere-2026-931
Preprint. Discussion started: 9 March 2026

Dutrieux, P., Vaughan, D. G., Corr, H. F., Jenkins, A., Holland, P. R., Joughin, I., and Fleming, A. H.: Pine Island Glacier Ice Shelf Melt Distributed at Kilometre Scales, Cryosphere, 7, 1543–1555, https://doi.org/10.5194/tc-7-1543-2013, 2013.

Dutrieux, P., De Rydt, J., Jenkins, A., Holland, P. R., Ha, H. K., Lee, S. H., Steig, E. J., Ding, Q., Abrahamsen, E. P., and Schröder, M.: Strong Sensitivity of Pine Island Ice-Shelf Melting to Climatic Variability, Science, 343, 174–178, https://doi.org/10.1126/science.1244341, 2014.

Edwards, T. L., Nowicki, S., Marzeion, B., Hock, R., Goelzer, H., Seroussi, H., Jourdain, N. C., Slater, D. A., Turner, F. E., Smith, C. J., McKenna, C. M., Simon, E., Abe-Ouchi, A., Gregory, J. M., Larour, E., Lipscomb, W. H., Payne, A. J., Shepherd, A., Agosta, C., Alexander, P., Albrecht, T., Anderson, B., Asay-Davis, X., Aschwanden, A., Barthel, A., Bliss, A., Calov, R., Chambers, C., Champollion, N., Choi, Y., Cullather, R., Cuzzone, J., Dumas, C., Felikson, D., Fettweis, X., Fujita, K., Galton-Fenzi, B. K., Gladstone, R., Golledge, N. R., Greve, R., Hattermann, T., Hoffman, M. J., Humbert, A., Huss, M., Huybrechts, P., Immerzeel, W., Kleiner, T., Kraaijenbrink, P., Le clec'h, S., Lee, V., Leguy, G. R., Little, C. M., Lowry, D. P., Malles, J.-H., Martin, D. F., Maussion, F., Morlighem, M., O'Neill, J. F., Nias, I., Pattyn, F., Pelle, T., Price, S. F., Quiquet, A., Radić, V., Reese, R., Rounce, D. R., Rückamp, M., Sakai, A., Shafer, C., Schlegel, N.-J., Shannon, S., Smith, R. S., Straneo, F., Sun, S., Tarasov, L., Trusel, L. D., Van Breedam, J., van de Wal, R., van den Broeke, M., Winkelmann, R., Zekollari, H., Zhao, C., Zhang, T., and Zwinger, T.: Projected Land Ice Contributions to Twenty-First-Century Sea Level Rise, Nature, 593, 74–82, https://doi.org/10.1038/s41586-021-03302-y, 2021.

Engwirda, D.: Locally Optimal Delaunay-refinement and Optimisation-Based Mesh Generation, 2014.

Favier, L., Pattyn, F., Berger, S., and Drews, R.: Dynamic Influence of Pinning Points on Marine Ice-Sheet Stability: A Numerical Study in Dronning Maud Land, East Antarctica, Cryosphere, 10, 2623–2635, https://doi.org/10.5194/tc-10-2623-2016, 2016.

Favier, L., Jourdain, N. C., Jenkins, A., Merino, N., Durand, G., Gagliardini, O., Gillet-Chaulet, F., and Mathiot, P.: Assessment of Sub-Shelf Melting Parameterisations Using the Ocean-Ice-Sheet Coupled Model NEMO(v3.6)-Elmer/Ice(v8.3), Geoscientific Model Development, 12, 2255–2283, https://doi.org/10.5194/gmd-12-2255-2019, 2019.

Fricker, H. A., Coleman, R., Padman, L., Scambos, T. A., Bohlander, J., and Brunt, K. M.: Mapping the Grounding Zone of the Amery Ice Shelf, East Antarctica Using InSAR, MODIS and ICESat, Antarctic Science, 21, 515–532, https://doi.org/10.1017/S095410200999023X, 2009.

Gagliardini, O., Durand, G., Zwinger, T., Hindmarsh, R. C. A., and Le Meur, E.: Coupling of Ice-Shelf Melting and Buttressing Is a Key Process in Ice-Sheets Dynamics, Geophysical Research Letters, 37, https://doi.org/10.1029/2010GL043334, 2010.

Getraer, B. and Morlighem, M.: Increasing the Glen–Nye Power-Law Exponent Accelerates Ice-Loss Projections for the Amundsen Sea Embayment, West Antarctica, Geophysical Research Letters, 52, e2024GL112 516, https://doi.org/https://doi.org/10.1029/2024GL112516, e2024GL112516 2024GL112516, 2025.

Goldberg, D. N. and Holland, P. R.: The Relative Impacts of Initialization and Climate Forcing in Coupled Ice Sheet-Ocean Modeling: Application to Pope, Smith, and Kohler Glaciers, Journal of Geophysical Research: Earth Surface, 127, e2021JF006 570, https://doi.org/10.1029/2021JF006570, 2022.

Goldberg, D. N., Gourmelen, N., Kimura, S., Millan, R., and Snow, K.: How Accurately Should We Model Ice Shelf Melt Rates?, Geophysical Research Letters, 46, 189–199, https://doi.org/10.1029/2018GL080383, 2019.

Gourmelen, N., Jakob, L., Holland, P. R., Dutrieux, P., Goldberg, D., Bevan, S., Luckman, A., and Malczyk, G.: The Influence of Subglacial Lake Discharge on Thwaites Glacier Ice-Shelf Melting and Grounding-Line Retreat, Nature Communications, 16, 2272, https://doi.org/10.1038/s41467-025-57417-1, 2025.

Greene, C. A., Gardner, A. S., Schlegel, N.-J., and Fraser, A. D.: Antarctic Calving Loss Rivals Ice-Shelf Thinning, Nature, 609, 948–953, https://doi.org/10.1038/s41586-022-05037-w, 2022.

https://doi.org/10.5194/egusphere-2026-931
Preprint. Discussion started: 9 March 2026

Gudmundsson, G. H., Krug, J., Durand, G., Favier, L., and Gagliardini, O.: The Stability of Grounding Lines on Retrograde Slopes, The Cryosphere, 6, 1497–1505, https://doi.org/10.5194/tc-6-1497-2012, 2012.

Gudmundsson, G. H., Paolo, F. S., Adusumilli, S., and Fricker, H. A.: Instantaneous Antarctic Ice Sheet Mass Loss Driven by Thinning Ice Shelves, Geophysical Research Letters, 46, 13 903–13 909, https://doi.org/10.1029/2019GL085027, 2019.

Gudmundsson, G. H., Barnes, J. M., Goldberg, D. N., and Morlighem, M.: Limited Impact of Thwaites Ice Shelf on Future Ice Loss From Antarctica, Geophysical Research Letters, 50, e2023GL102 880, https://doi.org/10.1029/2023GL102880, 2023.

Gwyther, D. E., Kusahara, K., Asay-Davis, X. S., Dinniman, M. S., and Galton-Fenzi, B. K.: Vertical Processes and Resolution Impact Ice Shelf Basal Melting: A Multi-Model Study, Ocean Modelling, 147, 101 569, https://doi.org/10.1016/j.ocemod.2020.101569, 2020.

Haigh, M. and Holland, P. R.: Decadal Variability of Ice-Shelf Melting in the Amundsen Sea Driven by Sea-Ice Freshwater Fluxes, Geophysical Research Letters, 51, e2024GL108 406, https://doi.org/10.1029/2024GL108406, 2024.

Haigh, M., Holland, P. R., Harrison, T. C., and Dutrieux, P.: Wind-Driven Coastal Polynya Variability Drives Decadal Ice-Shelf Melt Variability in the Amundsen Sea, Geophysical Research Letters, 53, e2025GL118 546, https://doi.org/10.1029/2025GL118546, 2026.

Hellmer, H. and Olbers, D.: A two-dimensional model for the thermohaline circulation under an ice shelf, Antarctic Science, 1, 325–336, https://doi.org/10.1017/S0954102089000490, 1989.

Holland, D. M. and Jenkins, A.: Modeling Thermodynamic Ice-Ocean Interactions at the Base of an Ice Shelf, Journal of Physical Oceanography, 29, 1787–1800, 1999.

Holland, P. R., Bevan, S. L., and Luckman, A. J.: Strong Ocean Melting Feedback During the Recent Retreat of Thwaites Glacier, Geophysical Research Letters, 50, e2023GL103 088, https://doi.org/10.1029/2023GL103088, 2023.

Jacobs, S. S., Hellmer, H. H., and Jenkins, A.: Antarctic Ice Sheet Melting in the Southeast Pacific, Geophysical Research Letters, 23, 957–960, 1996.

Jenkins, A., Nicholls, K. W., and Corr, H. F.: Observation and Parameterization of Ablation at the Base of Ronne Ice Shelf, Antarctica, Journal of Physical Oceanography, 40, 2298–2312, https://doi.org/10.1175/2010JPO4317.1, 2010.

Jenkins, A., Dutrieux, P., Jacobs, S., Steig, E. J., Gudmundsson, G. H., Smith, J., and Heywood, K. J.: Decadal Ocean Forcing and Antarctic Ice Sheet Response: Lessons from the Amundsen Sea, Oceanography, 29, 106–117, https://doi.org/10.5670/oceanog.2016.103, 2016.

Joughin, I., Shapero, D., Smith, B., Dutrieux, P., and Barham, M.: Ice-Shelf Retreat Drives Recent Pine Island Glacier Speedup, Science Advances, 7, 3080–3091, https://doi.org/10.1126/sciadv.abg3080, 2021.

Jourdain, N. C., Mathiot, P., Merino, N., Durand, G., Le Sommer, J., Spence, P., Dutrieux, P., and Madec, G.: Ocean Circulation and Sea-Ice Thinning Induced by Melting Ice Shelves in the Amundsen Sea, Journal of Geophysical Research: Oceans, 122, 2550–2573, https://doi.org/10.1002/2016JC012509, 2017.

Kimura, S., Jenkins, A., Regan, H., Holland, P. R., Assmann, K. M., Whitt, D. B., Van Wessem, M., van de Berg, W. J., Reijmer, C. H., and Dutrieux, P.: Oceanographic Controls on the Variability of Ice-Shelf Basal Melting and Circulation of Glacial Meltwater in the Amundsen Sea Embayment, Antarctica, Journal of Geophysical Research: Oceans, 122, 10 131–10 155, https://doi.org/10.1002/2017JC012926, 2017.

Konrad, H., Shepherd, A., Gilbert, L., Hogg, A. E., McMillan, M., Muir, A., and Slater, T.: Net Retreat of Antarctic Glacier Grounding Lines, Nature Geoscience, 11, 258–262, https://doi.org/10.1038/s41561-018-0082-z, 2018.

Lhermitte, S., Sun, S., Shuman, C., Wouters, B., Pattyn, F., Wuite, J., Berthier, E., and Nagler, T.: Damage Accelerates Ice Shelf Instability and Mass Loss in Amundsen Sea Embayment, Proceedings of the National Academy of Sciences of the United States of America, 117, 24 735–24 741, https://doi.org/10.1073/pnas.1912890117, 2020.

https://doi.org/10.5194/egusphere-2026-931
Preprint. Discussion started: 9 March 2026

Losch, M.: Modeling Ice Shelf Cavities in a z Coordinate Ocean General Circulation Model, Journal of Geophysical Research: Oceans, 113, https://doi.org/10.1029/2007JC004368, 2008.

Lowry, D. P., Krapp, M., Golledge, N. R., and Alevropoulos-Borrill, A.: The Influence of Emissions Scenarios on Future Antarctic Ice Loss Is Unlikely to Emerge This Century, Communications Earth & Environment, 2, 1–14, https://doi.org/10.1038/s43247-021-00289-2, 2021.

Macayeal, D. R.: Large-Scale Ice Flow over a Viscous Basal Sediment: Theory and Application to Ice Stream B, Antarctica, Journal of Geophysical Research, 94, 4071–4087, https://doi.org/10.1029/jb094ib04p04071, 1989.

Marshall, J., Hill, C., Perelman, L., and Adcroft, A.: Hydrostatic, Quasi-Hydrostatic, and Nonhydrostatic Ocean Modeling, Journal of Geophysical Research: Oceans, 102, 5733–5752, https://doi.org/10.1029/96JC02776, 1997.

Mathiot, P. and Jourdain, N. C.: Southern Ocean Warming and Antarctic Ice Shelf Melting in Conditions Plausible by Late 23rd Century in a High-End Scenario, Ocean Science, 19, 1595–1615, https://doi.org/10.5194/os-19-1595-2023, 2023.

McPhee, M. G., Maykut, G. A., and Morison, J. H.: Dynamics and Thermodynamics of the Ice/Upper Ocean System in the Marginal Ice Zone of the Greenland Sea, Journal of Geophysical Research: Oceans, 92, 7017–7031, https://doi.org/10.1029/JC092iC07p07017, 1987.

Melchior Van Wessem, J., Jan Van De Berg, W., Noël, B. P., Van Meijgaard, E., Amory, C., Birnbaum, G., Jakobs, C. L., Krüger, K., Lenaerts, J. T., Lhermitte, S., Ligtenberg, S. R., Medley, B., Reijmer, C. H., Van Tricht, K., Trusel, L. D., Van Ulft, L. H., Wouters, B., Wuite, J., and Van Den Broeke, M. R.: Modelling the Climate and Surface Mass Balance of Polar Ice Sheets Using RACMO2 - Part 2: Antarctica (1979-2016), Cryosphere, 12, 1479–1498, https://doi.org/10.5194/tc-12-1479-2018, 2018.

Milillo, P., Rignot, E., Rizzoli, P., Scheuchl, B., Mouginot, J., Bueso-Bello, J., and Prats-Iraola, P.: Heterogeneous Retreat and Ice Melt of Thwaites Glacier, West Antarctica, Science Advances, 5, eaau3433, https://doi.org/10.1126/sciadv.aau3433, 2019.

Milillo, P., Rignot, E., Rizzoli, P., Scheuchl, B., Mouginot, J., Bueso-Bello, J. L., Prats-Iraola, P., and Dini, L.: Rapid Glacier Retreat Rates Observed in West Antarctica, Nature Geoscience, 15, 48–53, https://doi.org/10.1038/s41561-021-00877-z, 2022.

Morlighem, M., Rignot, E., Binder, T., Blankenship, D., Drews, R., Eagles, G., Eisen, O., Ferraccioli, F., Forsberg, R., Fretwell, P., Goel, V., Greenbaum, J. S., Gudmundsson, H., Guo, J., Helm, V., Hofstede, C., Howat, I., Humbert, A., Jokat, W., Karlsson, N. B., Lee, W. S., Matsuoka, K., Millan, R., Mouginot, J., Paden, J., Pattyn, F., Roberts, J., Rosier, S., Ruppel, A., Seroussi, H., Smith, E. C., Steinhage, D., Sun, B., den Broeke, M. R., Ommen, T. D., van Wessem, M., and Young, D. A.: Deep Glacial Troughs and Stabilizing Ridges Unveiled beneath the Margins of the Antarctic Ice Sheet, Nature Geoscience, 13, 132–137, https://doi.org/10.1038/s41561-019-0510-8, 2020.

Morlighem, M., Goldberg, D., Dias dos Santos, T., Lee, J., and Sagebaum, M.: Mapping the Sensitivity of the Amundsen Sea Embayment to Changes in External Forcings Using Automatic Differentiation, Geophysical Research Letters, 48, https://doi.org/10.1029/2021GL095440, 2021.

Mouginot, J., Rignot, E., and Scheuchl, B.: MEaSUREs Annual Antarctic Ice Velocity Maps, Version 1, https://doi.org/10.5067/9T4EPQXTJYW9, 2017a.

Mouginot, J., Rignot, E., Scheuchl, B., and Millan, R.: Comprehensive Annual Ice Sheet Velocity Mapping Using Landsat-8, Sentinel-1, and RADARSAT-2 Data, Remote Sensing 2017, Vol. 9, Page 364, 9, 364, https://doi.org/10.3390/RS9040364, 2017b.

Mouginot, J., Scheuchl, B., and Rignot, E.: MEaSUREs Antarctic Boundaries for IPY 2007-2009 from Satellite Radar, Version 2, https://doi.org/10.5067/AXE4121732AD, 2017c.

Nakayama, Y., Menemenlis, D., Schodlok, M., and Rignot, E.: Amundsen and Bellingshausen Seas Simulation with Optimized Ocean, Sea Ice, and Thermodynamic Ice Shelf Model Parameters, Journal of Geophysical Research: Oceans, 122, 6180–6195, https://doi.org/10.1002/2016JC012538, 2017.

https://doi.org/10.5194/egusphere-2026-931
Preprint. Discussion started: 9 March 2026

Nakayama, Y., Menemenlis, D., Zhang, H., Schodlok, M., and Rignot, E.: Origin of Circumpolar Deep Water Intruding onto the Amundsen and Bellingshausen Sea Continental Shelves, Nature Communications, 9, https://doi.org/10.1038/s41467-018-05813-1, 2018.

Naughten, K. A., De Rydt, J., Rosier, S. H. R., Jenkins, A., Holland, P. R., and Ridley, J. K.: Two-Timescale Response of a Large Antarctic Ice Shelf to Climate Change, Nature Communications, 12, 1991, https://doi.org/10.1038/s41467-021-22259-0, 2021.

Naughten, K. A., Holland, P. R., Dutrieux, P., Kimura, S., Bett, D. T., and Jenkins, A.: Simulated Twentieth-Century Ocean Warming in the Amundsen Sea, West Antarctica, Geophysical Research Letters, 49, https://doi.org/10.1029/2021gl094566, 2022.

Naughten, K. A., Holland, P. R., and De Rydt, J.: Unavoidable Future Increase in West Antarctic Ice-Shelf Melting over the Twenty-First Century, Nature Climate Change, pp. 1–7, https://doi.org/10.1038/s41558-023-01818-x, 2023.

Nias, I. J., Cornford, S. L., Edwards, T. L., Gourmelen, N., and Payne, A. J.: Assessing Uncertainty in the Dynamical Ice Response to Ocean Warming in the Amundsen Sea Embayment, West Antarctica, Geophysical Research Letters, 46, 11 253–11 260, https://doi.org/10.1029/2019GL084941, 2019.

Nilsson, J., Gardner, A. S., and Paolo, F. S.: Elevation Change of the Antarctic Ice Sheet: 1985 to 2020, Earth System Science Data, 14, 3573–3598, https://doi.org/10.5194/essd-14-3573-2022, 2022.

Otosaka, I. N., Shepherd, A., Ivins, E. R., Schlegel, N.-J., Amory, C., Van Den Broeke, M. R., Horwath, M., Joughin, I., King, M. D., Krinner, G., Nowicki, S., Payne, A. J., Rignot, E., Scambos, T., Simon, K. M., Smith, B. E., Sørensen, L. S., Velicogna, I., Whitehouse, P. L., 10, G. A., Agosta, C., Ahlstrøm, A. P., Blazquez, A., Colgan, W., Engdahl, M. E., Fettweis, X., Forsberg, R., Gallée, H., Gardner, A., Gilbert, L., Gourmelen, N., Groh, A., Gunter, B. C., Harig, C., Helm, V., Khan, A., Kittel, C., Konrad, H., Langen, P. L., Lecavalier, B. S., Liang, C.-C., Loomis, B. D., Mcmillan, M., Melini, D., Mernild, S. H., Mottram, R., Mouginot, J., Nilsson, J., Noël, B., Pattle, M. E., Peltier, W. R., Pie, N., Roca, M., Sasgen, I., Save, H. V., Seo, K.-W., Scheuchl, B., Schrama, E. J. O., Schröder, L., Simonsen, S. B., Slater, T., Spada, G., Sutterley, T. C., Dutt Vishwakarma, B., Melchior Van Wessem, J., Wiese, D., Van Der Wal, W., and Wouters, B.: Mass Balance of the Greenland and Antarctic Ice Sheets from 1992 to 2020, Earth Syst. Sci. Data, 15, 1597–1616, https://doi.org/10.5194/essd-15-1597-2023, 2023.

Paolo, F. S., Gardner, A. S., Greene, C. A., Nilsson, J., Schodlok, M. P., Schlegel, N.-J., and Fricker, H. A.: Widespread Slowdown in Thinning Rates of West Antarctic Ice Shelves, The Cryosphere, 17, 3409–3433, https://doi.org/10.5194/tc-17-3409-2023, 2023.

Reed, B., Green, J. A. M., Jenkins, A., and Gudmundsson, G. H.: Melt Sensitivity of Irreversible Retreat of Pine Island Glacier, The Cryosphere, 18, 4567–4587, https://doi.org/10.5194/tc-18-4567-2024, 2024.

Reese, R., Gudmundsson, G. H., Levermann, A., and Winkelmann, R.: The Far Reach of Ice-Shelf Thinning in Antarctica, Nature Climate Change, 8, 53–57, https://doi.org/10.1038/s41558-017-0020-x, 2018.

Richter, O., Timmermann, R., Gudmundsson, G. H., and De Rydt, J.: Coupling Framework (1.0) for the Úa (2023b) Ice Sheet Model and the FESOM-1.4 z-Coordinate Ocean Model in an Antarctic Domain, Geoscientific Model Development, 18, 2945–2960, https://doi.org/10.5194/gmd-18-2945-2025, 2025.

Rignot, E., Mouginot, J., Morlighem, M., Seroussi, H., and Scheuchl, B.: Widespread, Rapid Grounding Line Retreat of Pine Island, Thwaites, Smith, and Kohler Glaciers, West Antarctica, from 1992 to 2011, Geophysical Research Letters, 41, 3502–3509, https://doi.org/10.1002/2014GL060140, 2014.

Rignot, E., Mouginot, J., and Scheuchl, B.: MEaSUREs InSAR-Based Antarctica Ice Velocity Map, Version 2, Boulder, Colorado USA, NASA National Snow and Ice Data Center Distributed Active Archive Center [data set], https://doi.org/10.5067/D7GK8F5J8M8R, 2017.

https://doi.org/10.5194/egusphere-2026-931
Preprint. Discussion started: 9 March 2026

Rignot, E., Mouginot, J., Scheuchl, B., van den Broeke, Michiel., van Wessem, Melchior. J., and Morlighem, M.: Four Decades of Antarctic Ice Sheet Mass Balance from 1979–2017, Proceedings of the National Academy of Sciences, 116, 1095–1103, https://doi.org/10.1073/pnas.1812883116, 2019.

Ritz, C., Edwards, T. L., Durand, G., Payne, A. J., Peyaud, V., and Hindmarsh, R. C.: Potential Sea-Level Rise from Antarctic Ice-Sheet Instability Constrained by Observations, Nature, 528, 115–118, https://doi.org/10.1038/nature16147, 2015.

Rosier, S. H. R., Gudmundsson, G. H., Jenkins, A., and Naughten, K. A.: Calibrated Sea Level Contribution from the Amundsen Sea Sector, West Antarctica, under RCP8.5 and Paris 2C Scenarios, The Cryosphere, 19, 2527–2557, https://doi.org/10.5194/tc-19-2527-2025, 2025.

Ross, N., Milillo, P., and Dini, L.: Antarctic grounding line delineation from the Italian Space Agency COSMO-SkyMed DInSAR data, Scientific Data, 12, 1737, 2025.

Schelpe, C. A. O. and Gudmundsson, G. H.: Incorporating Horizontal Density Variations Into Large-Scale Modeling of Ice Masses, Journal of Geophysical Research: Earth Surface, 128, e2022JF006 744, https://doi.org/https://doi.org/10.1029/2022JF006744, e2022JF006744 2022JF006744, 2023.

Seroussi, H., Nakayama, Y., Larour, E., Menemenlis, D., Morlighem, M., Rignot, E., and Khazendar, A.: Continued Retreat of Thwaites Glacier, West Antarctica, Controlled by Bed Topography and Ocean Circulation, Geophysical Research Letters, 44, 6191–6199, https://doi.org/10.1002/2017GL072910, 2017.

Seroussi, H., Nowicki, S., Simon, E., Abe-Ouchi, A., Albrecht, T., Brondex, J., Cornford, S., Dumas, C., Gillet-Chaulet, F., Goelzer, H., Golledge, N. R., Gregory, J. M., Greve, R., Hoffman, M. J., Humbert, A., Huybrechts, P., Kleiner, T., Larour, E., Leguy, G., Lipscomb, W. H., Lowry, D., Mengel, M., Morlighem, M., Pattyn, F., Payne, A. J., Pollard, D., Price, S. F., Quiquet, A., Reerink, T. J., Reese, R., Rodehacke, C. B., Schlegel, N.-J., Shepherd, A., Sun, S., Sutter, J., Van Breedam, J., van de Wal, R. S. W., Winkelmann, R., and Zhang, T.: initMIP-Antarctica: An Ice Sheet Model Initialization Experiment of ISMIP6, The Cryosphere, 13, 1441–1471, https://doi.org/10.5194/tc-13-1441-2019, 2019.

Seroussi, H., Pelle, T., Lipscomb, W. H., Abe-Ouchi, A., Albrecht, T., Alvarez-Solas, J., Asay-Davis, X., Barre, J.-B., Berends, C. J., Bernales, J., Blasco, J., Caillet, J., Chandler, D. M., Coulon, V., Cullather, R., Dumas, C., Galton-Fenzi, B. K., Garbe, J., Gillet-Chaulet, F., Gladstone, R., Goelzer, H., Golledge, N., Greve, R., Gudmundsson, G. H., Han, H. K., Hillebrand, T. R., Hoffman, M. J., Huybrechts, P., Jourdain, N. C., Klose, A. K., Langebroek, P. M., Leguy, G. R., Lowry, D. P., Mathiot, P., Montoya, M., Morlighem, M., Nowicki, S., Pattyn, F., Payne, A. J., Quiquet, A., Reese, R., Robinson, A., Saraste, L., Simon, E. G., Sun, S., Twarog, J. P., Trusel, L. D., Urruty, B., Van Breedam, J., van de Wal, R. S. W., Wang, Y., Zhao, C., and Zwinger, T.: Evolution of the Antarctic Ice Sheet Over the Next Three Centuries From an ISMIP6 Model Ensemble, Earth's Future, 12, e2024EF004 561, https://doi.org/10.1029/2024EF004561, 2024.

Shean, D. E., Joughin, I. R., Dutrieux, P., Smith, B. E., and Berthier, E.: Ice Shelf Basal Melt Rates from a High-Resolution Digital Elevation Model (DEM) Record for Pine Island Glacier, Antarctica, Cryosphere, 13, 2633–2656, https://doi.org/10.5194/tc-13-2633-2019, 2019.

Shepherd, A., Gilbert, L., Muir, A. S., Konrad, H., McMillan, M., Slater, T., Briggs, K. H., Sundal, A. V., Hogg, A. E., and Engdahl, M. E.: Trends in Antarctic Ice Sheet Elevation and Mass, Geophysical Research Letters, 46, 8174–8183, https://doi.org/10.1029/2019GL082182, 2019.

Silvano, A., Holland, P. R., Naughten, K. A., Dragomir, O., Dutrieux, P., Jenkins, A., Si, Y., Stewart, A. L., Peña Molino, B., Janzing, G. W., Dotto, T. S., and Naveira Garabato, A. C.: Baroclinic Ocean Response to Climate Forcing Regulates Decadal Variability of Ice-Shelf Melting in the Amundsen Sea, Geophysical Research Letters, 49, e2022GL100 646, https://doi.org/10.1029/2022GL100646, 2022.

https://doi.org/10.5194/egusphere-2026-931
Preprint. Discussion started: 9 March 2026

Smith, B., Fricker, H. A., Gardner, A. S., Medley, B., Nilsson, J., Paolo, F. S., Holschuh, N., Adusumilli, S., Brunt, K., Csatho, B., Harbeck, K., Markus, T., Neumann, T., Siegfried, M. R., and Zwally, H. J.: Pervasive Ice Sheet Mass Loss Reflects Competing Ocean and Atmosphere Processes, Tech. rep., 2020.

Sun, S. and Gudmundsson, G. H.: The Speedup of Pine Island Ice Shelf between 2017 and 2020: Revaluating the Importance of Ice Damage, Journal of Glaciology, pp. 1–9, https://doi.org/10.1017/jog.2023.76, 2023.

Surawy-Stepney, T., Hogg, A. E., Cornford, S. L., and Davison, B. J.: Episodic Dynamic Change Linked to Damage on the Thwaites Glacier Ice Tongue, Nature Geoscience, 16, 37–43, https://doi.org/10.1038/s41561-022-01097-9, 2023.

Turner, K. A., Naughten, K. A., Holland, P. R., and Naveira Garabato, A. C.: Modeled Centennial Ocean Warming in the Amundsen Sea Driven by Thermodynamic Atmospheric Changes, Not Winds, Geophysical Research Letters, 52, e2024GL112 287, https://doi.org/10.1029/2024GL112287, 2025.

Walker, D. P., Jenkins, A., Assmann, K. M., Shoosmith, D. R., and Brandon, M. A.: Oceanographic Observations at the Shelf Break of the Amundsen Sea, Antarctica, Journal of Geophysical Research: Oceans, 118, 2906–2918, https://doi.org/10.1002/jgrc.20212, 2013.

Wang, S., Alexander, P. M., Alley, R. B., Huang, Z., Parizek, B. R., Willet, A. G., and Anandakrishnan, S.: Recent Variability in Fracture Characteristics and Ice Flow of Thwaites Ice Shelf, West Antarctica, Journal of Geophysical Research: Earth Surface, 130, e2024JF008 118, https://doi.org/10.1029/2024JF008118, 2025.

Wild, C. T., Alley, K. E., Muto, A., Truffer, M., Scambos, T. A., and Pettit, E. C.: Weakening of the Pinning Point Buttressing Thwaites Glacier, West Antarctica, The Cryosphere, 16, 397–417, https://doi.org/10.5194/tc-16-397-2022, 2022.